Colorimetric description of thermochromic printing inks

Maja Jakovljević[1], Rahela Kulčar[1], Dario Tomašegović[1], Mojca Friškovec[2], Marta Klanjšek Gunde[3]

[1] University of Zagreb, Faculty of Graphic Arts, Getaldićeva 2, Zagreb, Croatia

[2] Cetis, Graphic and Documentation Services, d.d., Čopova 24, Celje, Slovenia

[3] National Institute of Chemistry, Ljubljana, Hajdrihova 19, Slovenia

Abstract

The dynamic colour of three commercial reversible thermochromic inks were studied. Thermochromic printing inks change their colour according to a change in temperature. The two types of thermochromic inks are based on leuco dyes and liquid crystals. The thermochromic effect achieved by liquid crystals is quite different from the effect achieved with leuco dyes. Leuco dyes change from a coloured to a colourless state, or from one colour shade to another due to structural changes inside leuco dye molecules under assistance of developer. Liquid crystal inks change colour continuously throughout the spectrum, producing iridescent colours starting from red and shifting to blue part of the spectrum with temperature. The colour change results from the way light interacts with special arrangement of liquid crystal molecules to produce coloured reflection by interference, and with the variation of this structure with temperature. In this paper we will present differences between two types of thermochromic printing inks giving careful colorimetric characterization.

Keywords: Thermochromic inks, leuco dye, liquid crystals, colorimetric properties

1.   Introduction

Thermochromic (TC) inks constitute one of the major groups of colour changing inks. Colour - changing inks are becoming increasingly important in various applications for smart packaging, security printing, brand protection, medical applications, marketing, toys and textile colouring (Johansson, 2006; White and LeBlanc, 1999; Phillips, 2000; Christie, 2007; Seeboth and Lötzsch, 2008; Worbin, 2010). The main purpose of such application is to carry and protect the product as well as to market it.

In most cases, the colour change occurs inside the microcapsules containing thermo - responsive materials (Seeboth and Lötzsch, 2008; White and Leblanc, 1999). There are two basic types of thermo - responsive materials, leucodye - based composites (TLDs) and thermochromic liquid crystals (TLCs) (see Figure 1). The colour change occurs at the defined activation temperature T_A (for TLDs) and in the activation region (for TLCs).

Leucodye - based inks usually change from coloured to discoloured state above the activation temperature (T_A), where the name originates from (λευκος in greek: white) (Jakovljević et al., 2016). However, in some cases the printing ink is formulated to change from one colour to another by careful selection of dye (Bamfield and Hutchings, 2010). Thermochromic composites in leucodye - based inks consist of a leuco dye (colour former), colour developer and organic solvent. The colour changes due to the structural modifications as a function of temperature (Tang et al., 2010; Zhu and Wu, 2005). To achieve the desired effect the components are mixed in specific ratios and usually encapsulated to protect the system in subsequent applications. The colour change effect of the TLDs occurs at the defined T_A and is in most cases reversible; in special situations also irreversible TLDs are possible.

Reversible TLD printing inks in most cases change from coloured to colourless state as the

temperature is raised above the T_A and recolor again when cooled well below it (see Figure 1a). T_A is determined by the temperature where the solvent applied to prepare TLDs changes from solid to liquid state, causing the colour - forming components to form a colour complex below the transition temperature (coloured state) and destroyed it above this temperature (discoloured state) (Gunde et al., 2011; Kulčar et al., 2010; MacLaren and White, 2003). Microencapsulated TLDs are applied in commercial inks with various T_A, from -15°C up to 65°C. TLD inks of all basic types are available, such as water - based, solvent - based and photocuring inks for screen- and offset printing on paper, plastics, metal and textile. They are frequently mixed with conventional inks to obtain an interchange between the two single colours (Kulčar et al., 2011).

TLDs are easily applicable with practically no difference to conventional printing inks. Reversible TLD inks can be printed using flexography, screen gravure and offset printing methods.
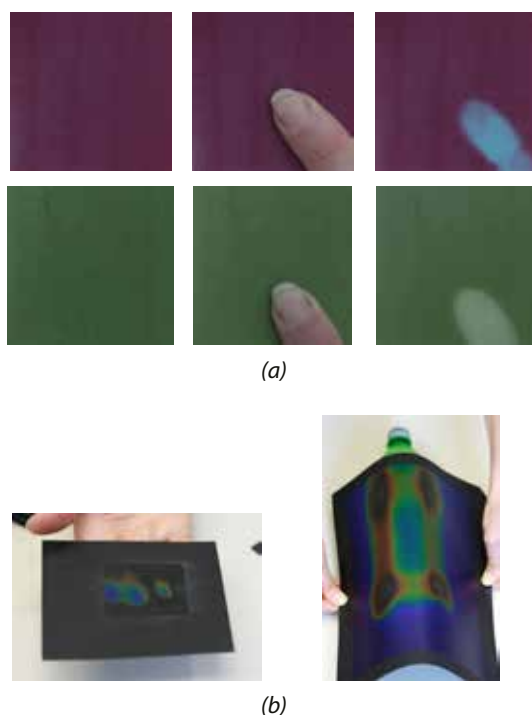

(a)

(b)

Figure 1. Colour change on printed samples with thermochromic leuco dyes (a) and thermochromic liquid crystals (b)

TLC printing inks start a colour change at the defined T_A, but the colour change occurs in several degrees wide region above the T_A. This

temperature range is called activation region but can also be called the colour play interval. Within the activation region colour changes throughout the whole visible spectrum from red, orange, yellow, green, blue to violet (rainbow, iridescent colour) (see Figure 1b). This effect is known as "colour play". TLC ink is colourless for the temperatures of the sample below or above the activation region. The transformation from colourless state to coloured one takes place gradually when temperature reaches the lower edge of the activation region. Above the upper edge of the activation region the purple colour fades until the TLC becomes colourless again. The temperature needed to reach the colourless stage is called "the clearing point" (Hallcrest, 2014; Jakovljević et al., 2016).

The active material in TLCs consists of elongated (rod - shaped) molecules that undergo phase changes from crystalline solid to isotropic liquid trough chiral nematic (or cholesteric) mesophase. Equally oriented molecules inside the adjacent sheets twist and the direction of the long axis of molecules traces out a helical path. Helical superstructure which is developed in chiral nematic or cholesteric mesophase (i.e. a special phase between the solid and liquid states of the material) causes special optical properties of TLC ink at temperatures inside the activation region. The degree of this effect is described by pitch length P; defined as the length of the pitch in the helix formed by 360° rotation of directions of elongated molecules of the TLC (see Figure 2). Optical effect of TLC printing inks is based on selective reflection of light from the helical structure, with P depending on temperature - if P is comparable to the wavelength of light that falls parallel to the axis of the helix, the light is reflected at a wavelength equal to the optical value of P. As the temperature rises the helical pitches shrink, causing reflections of light with shorter wavelengths (Hallcrest, 2014; Jakovljević et al., 2013; Sage, 2011). Therefore, the temperature dependent P causes the TC effect in TLCs.
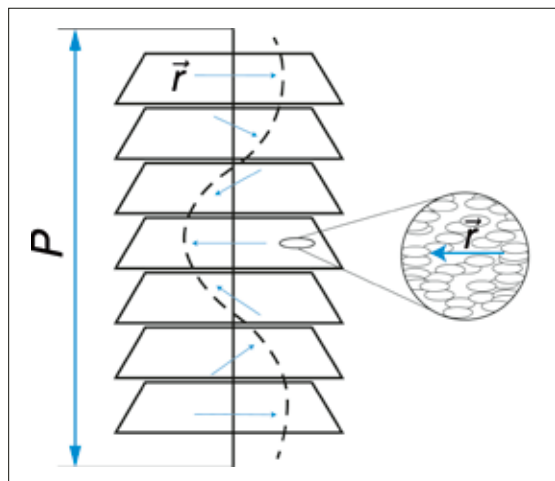
Figure 2. Helical superstructure of TLC-s (Hallcrest, 2014)

The active material in TLCs does not absorb the visible light, but reflects a narrow spectral region thus producing approximately monochromatic colour similar to colour of rainbow (i.e. iridescent colours). The colour play effect of the TLC inks is rather weak - most of the light transmits the material. This light could scatter on the substrate and largely obscure the light reflected on the molecular pitch. To prevent this, TLCs should be applied to black substrate which absorbs the transmitted light. Only under such circumstances, the iridescent colours can be seen (Jakovljević et al., 2013). The entire colour change occurs in a few degrees wide temperature range, which ensures TLCs to be much more sensitive to temperature changes then TLDs. They can have a versatile range of colour and useful colour changes between -30 and 100°C, often with very high temperature sensitivity (Sage, 2011; White and LeBlanc, 1999). The width of activation regions can vary between 1 and 20°C. The colour change of the most TLC inks is reversible (Hallcrest, 2014).

TLC printing inks are finding increasing use in applications such as temperature and packaging indicators, security printing and brand protection. An application area which has seen consistent focus is the use of thermochromic liquid crystals in engineering applications. The ability to monitor and map the temperature of a substantial area of surface can be a great advantage in detecting a fault or localising activity. In electronics, liquid crystals can be used to detect short circuits, open circuits, inoperative devices, and map operational areas in large - scale integrated circuits (Sage, 2011).

The active material of TC inks, whether it is leuco dye or liquid crystal, is in most cases microencapsulated, in order to protect the active material from negative impacts of the environment. Microcapsulation enables printing of thin layers of TC inks on almost any type of printing substrate. Printing thicker layers of TC inks is recommended for stronger TC effect and better resistance to UV light. Microcapsules of TC printing inks are dispersed in a suitable binder. The colour, mechanism of its change and temperature where the change occurs are determined by the material inside microcapsules whereas the binder defines the printing and curing technology (Seeboth and Lötzsch, 2008; White and LeBlanc, 1999).

The differences between TLD and TLC printing inks are presented here, giving careful characterization of temperature dependent colorimetric properties.

2. Experimental

The results obtained for commercially available TC inks are shown here. Three TC inks were used, from three different manufacturers and with different activation temperatures. The data given from the suppliers of these inks are given in Table 1.

Table 1: Basic data of the TC inks applied here: manufacturer, type of ink, printing technique, drying method and activation temperature/region.

Ink	TLC25	TLD63	TLD27
Manufacturer	Printcolor	CTI	LCRHallcrest
Type of ink	liquid crystals	leuco dye	leuco dye
Printing technique	screen	offset	offset
Drying	air	air	air
Activation (°C)	25	63	27

TLD inks were printed on Prüfbau MZ II Multipurpose Printability Testing Instrument over white uncoated paper (140 g/m²). TLD27 ink change colour from blue to colourless and TLD63 ink change from burgundy to blue colour.

The reflectance spectra were measured in three cycles. In each cycle the sample was heated from the lowest to the highest temperature and

then cooled back to the lowest one. Around the T_A the reflectance spectra were measured every 0.5°C or 1°C intervals. TLD27 was measured from 12°C to 40°C, TLD63 from 38°C to 74°C and TLC25 from 24°C to 45°C.

TLC25 (Printcolour Screen Ltd., Switzerland) water-based ink was screen - printed, using 149 µm mesh openings, on the black coated paper (260 g/m²). This ink was printed in two subsequent layers (wet over dry) and hot air dried at 75°C. T_A of the TLC ink was at 25°C and the activation region from 25°C to 30°C. Within the activation region the TLC ink showed the full "colour play" effect changing throughout the whole visible spectrum, with the effect being reversible. The ink was colourless outside the activation temperature. For the temperatures above the activation region the ink still showed some colour change, but the effect faded gradually till the complete loss of colour above 44°C (clearing point), becoming colourless again (Table 2).

Table 2. Technical specification of the TLC ink

TLC T_A	Red	Green	Blue	Clearing point
25°C	25°C	26°C	30°C	44°C

The measurements were obtained from the samples heated on the thermostatically controlled water inside water block (EK Water Blocks, EKWB, Slovenia). From the obtained reflectance spectra the corresponding CIELAB values were calculated and presented as (a^*, b^*), $L^*(T)$ and (L^*, C^*) graphs.

Spectrometer Ocean Optics USB2000+ with 50mm wide integrating sphere was used for measuring temperature - dependent colorimetric properties of the TC inks. Ocean Optics SpectraSuite software was used for the calculation of the CIELAB values L^*, a^*, b^* and C^* from measured reflectance. The D50 illuminant and 2° standard observer were applied in these calculation. The measurements were performed in the steps of 1 nm for the spectral region from 370 to 730 nm.

3. Results and discussion

The measured reflectance spectra of the samples printed with TLDs and TLCs are shown in Figs. 3–8. TLD27 sample become discoloured during heating and coloured again during cooling (Fig. 3, 4). TLD63 sample change from burgundy to

blue during heating and then back to burgundy during cooling (Fig. 5, 6). No abrupt change was observed and both processes are continuous. Decolourization of TLD27 is not complete even at the highest temperature applied in our experiment. This could be the result of incomplete transparency of the TC composite inside microcapsules at high temperature.

The reflectance spectra of TLC samples (Fig. 7) are completely different from that of TLDs. The effect of iridescent colour starts with rather broad reflectance peak with typical Lorentzian shape. Each individual spectrum show single reflectance peak. The peak in spectral reflection measured at 29°C peaks at 700 nm, so the colour play effect starts accordingly with the red colour. When temperature rises, the peak narrows and moves towards shorter wavelengths, i.e. from red colour further to orange, yellow, green, blue and purple. Above 40°C the colour play effect gradually declines and the colour fades approaching to the clearing point temperature. Due to black substrate and reflectance from cholesteric liquid crystal structure inside microcapsules of the TLC inks, spectral reflectance of TLC sample is much lower than spectral reflectance curves of TLD samples. The comparison of the three sets of reflectance curves is shown in Figure 8.
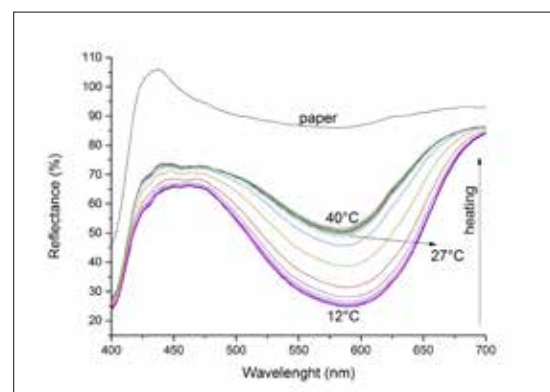

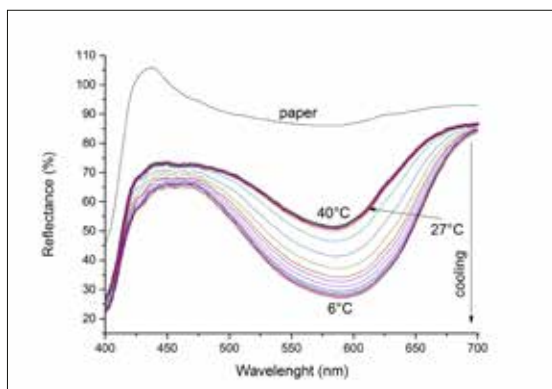**Figure 3. Spectral reflectance curves of TLD27, heating**

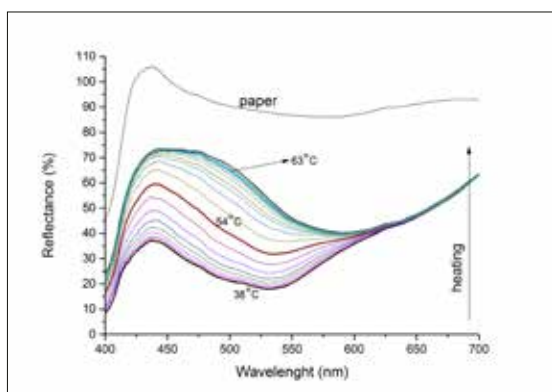**Figure 4. Spectral reflectance curves of TLD27, cooling**

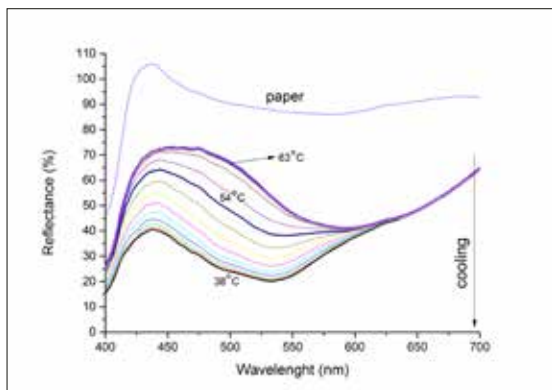**Figure 5. Spectral reflectance curves of TLD63, heating**

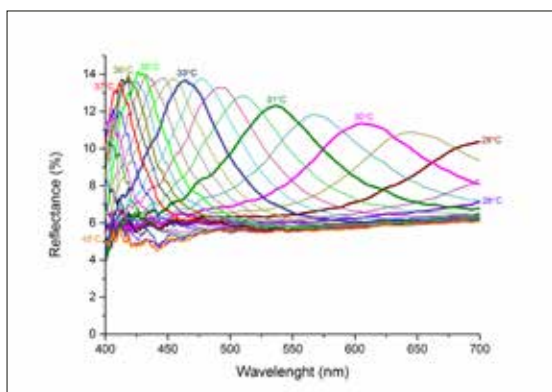**Figure 6. Spectral reflectance curves of TLD63, cooling**

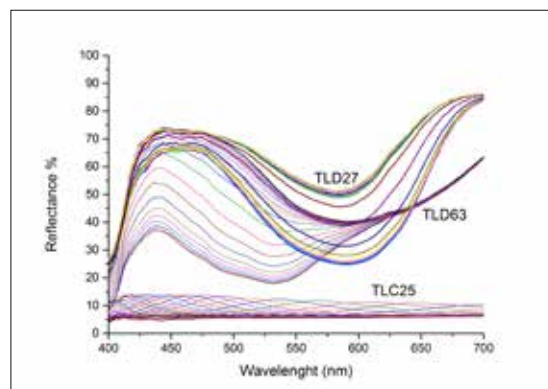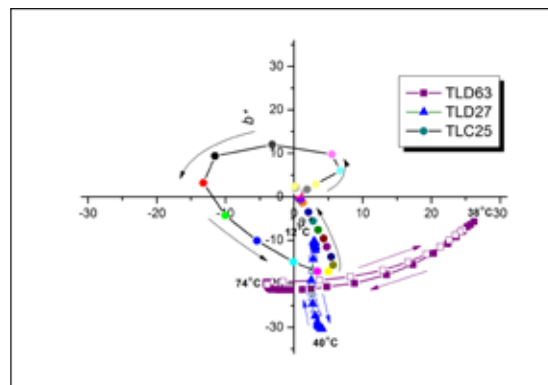**Figure 7. Spectral reflectance curves of TLC25, heating**

Figure 8. Spectral reflectance curves for three different TC inks (TLD27, TLD63 and TLC25), heating

The temperature dependent reflectance spectra were used for colorimetric analysis, to calculate the dependence of CIELAB values on temperature.

During heating/cooling cycle the a^*, b^*, L^*, and C^* values of a TC sample describe a path on the (a^*,b^*) and (L^*,C^*) planes (Fig. 9, 10). These paths of TLDs are in general not the same at heating and cooling, but differences are small.

TLC show completely different dynamical colour properties. When temperature rises from 25°C to 45°C the TLC ink continuously changes from transparent below T_A, followed by red, orange, yellow, green, blue and purple. As the rising temperature reaches the clearing point temperature (44°C), purple colour gradually fades until it completely disappears. Specific colour play effect of TLC printing inks describes the entire colour circle in (a^*,b^*) graph (Fig. 9). The shape of the curve demonstrates that the system was producing richer colours in green and blue regions than in the red region, which agrees with visual observation.

Figure 9. Changing of CIELAB values of TLD27, TLD63 and TLC25 samples in the (a*,b*) plane at heating (solid signs) and cooling (open signs).

The TLC describe practically closed loop which in all states remains at much lower L^* values than that of TLDs. Therefore, the two types of TC inks are clearly distinguishable in CIELAB colour space.
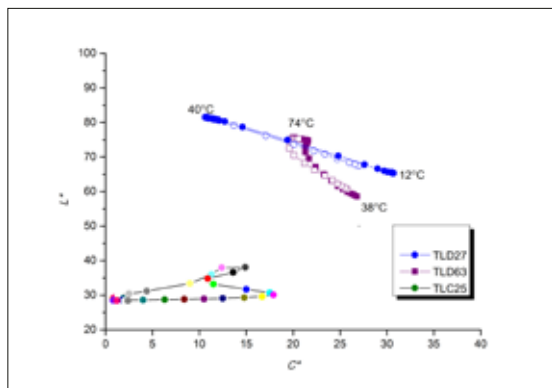

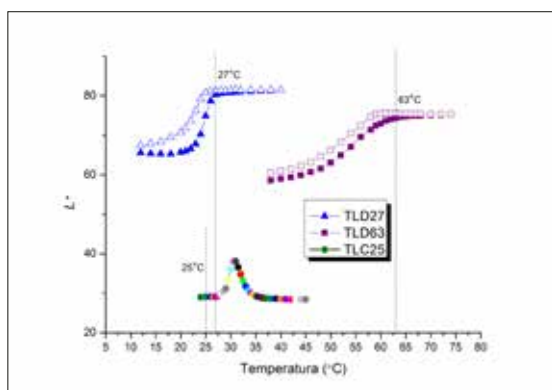**Figure 10. CIELAB (L*,C*) graphs of two TLDs and TLC ink**

Figure 11. CIELAB lightness L* of TLD27, TLD63 and TLC25 samples in dependence on temperature at heating (solid signs) and cooling (open signs)

The process is also illustrated by change of lightness L^* as a function of temperature (Figure 11). The TLDs entire L^*(T) curves have a form of a loop, known as hysteresis loop (Kulčar 2010). The TC system has a sort of memory-it is not possible to predict its output without knowing the path that it followed before the current state was reached. Such a phenomenon is called hysteresis. TC materials belong to several physical systems with hysteresis. It is colour hysteresis that describes the colour of a TC sample as a function of temperature.

The TLD samples do not show equal colour hysteresis: they differ in the temperatures where the loop starts and finishes. If a completely reversible process is assumed, a thermochromic sample should return to the same colour after

the whole heating/cooling cycle. Hysteresis loop of such a sample is closed.

The analysed TLC sample shows a single L^* peak with maximum at 30°C spreading over the entire activation region. At 25°C the L^* value is 29.1 and rises by further increase in temperature, reaching the maximum value at 30°C. Further temperature increase results in decreasing values of lightness, followed by a decline of the colour play effect. Above the clearing point temperature at 45°C the colour of the TLC completely fades. While the corresponding colour is essentially monochromatic (almost pure spectral colour are obtained) and changes with temperature over the visible spectral region, the L^*(T) curve cannot describe the colouration properties well enough and should be compared with other graphs, such as presented in Figures 9 and 10.

4. Conclusions

Thermo - responsive optical properties of two types of thermochromic printing inks presented in this research are very different. As the temperature is raised above the T_A, TLD printing inks change from coloured to colourless state and regain colour when cooled. TLD inks exibit colour as a result of selective absorption of light. Below activation temperature, i.e. in the coloured state, all effects are similar to that known for conventional inks. A light shade background is recommended when printing with TLD inks, since the TC composite is not opaque. If they are printed on a background colour other than white, the background colour will influence the colour of the ink. On the other hand, TLCs should be applied to black substrate - its high absorption prevents scattering of light which could obscure the weak reflection on TLCs.

Two analysed TLD samples show colour hysteresis: their colour does not depend only on temperature but also on the way this temperature was reached. A system with hysteresis has memory, i.e. it exhibits a path-dependence. The colour of samples prepared with a thermochromic ink is different when the same temperature is reached by heating or by cooling. Different colour hystereses were obtained. Printing inks based on TC leuco dyes are characterised by their relatively low accuracy (wide hysteresis

of temperature change). Therefore, functional applications of these inks tend to be for visual or indicative purpose only.

TLC printing inks provide special type of thermochromic effect inside the temperature activation region of the ink. The so-called colour play effect is based on selective reflectance of light from the helical structure of the TLCs. As the temperature rises, the colour play effect takes place inside temperature activation region of the ink, with the light being reflected in a narrow band within visible spectral region.

The presented research of temperature dependent colorimetric properties of thermochromic inks will contribute in understanding differences between leuco dye - based and liquid crystal - based printing inks. Although thermo - responsive properties are a common feature for both types of thermochromic printing inks, mechanism of the colour change differs in a great extent. As a result, each type of TC inks has specific temperature dependent colorimetric properties, which can determine the field of application for this functional materials. For this purpose the CIELAB values could be presented in (a^*,b^*) or (L^*,C^*) planes of the colour space. To provide an efficient application, the $L^*(T)$ graphs are also required.

5. References

Bamfield, P., Hutchings, M.G., 2010. Chromic Phenomena, 2nd Editio. ed, RSCPublishing.

Christie, R., 2007. Design concepts for a temperature-sensitive environment using thermochromic colour change. ColourDesign Creat. 1, 1–11.

Gunde, M.K., Friškovec, M., Kulčar, R., Hauptman, N., Kaplanova, M., Panak, O., Vesel, A., Klanj, M., Fri, M., Kul, R., Hauptman, N., Kaplanova, M., Panak, O., Vesel, A., 2011. Functional properties of the leuco dye-based thermochromic printing inks. In: 2011 Proceedings : "Disseminating Graphic Arts Research Internationally since 1948." Pittsburg, Pannsylvania, United States.

Hallcrest, 2014. Handbook of Thermochromic Liquid Crystal.

Jakovljević, M., Friškovec, M., Gunde, M.K., Lozo, B., 2013. Optical properties of thermochromic liquid crystal printing inks. In: Institute for Printing and Media Technology / Chemnitz University of Technology (Ed.), 5th International Scientific Conference on Print and Media Technology. Chemnitz, Germany, pp. 169–173.

Jakovljević, M., Lozo, B., Gunde, M.K., Arts, G., Arts, G., 2016. Packaging added value solutions by Thermochromic Liquid Crystal-based printed labels. In: Printing for Fabrication. IS&T, Manchester, UK, pp. 325–327.

Johansson, L., 2006. Creation of printed dynamic images. Linköping University.

Kulčar, R., Friškovec, M., Gunde, M.K., Knešaurek, N., 2011. Dynamic colorimetric properties of mixed thermochromic printing inks. Color. Technol. 127, 411–417.

Kulčar, R., Friškovec, M., Hauptman, N., Vesel, A., Gunde, M.K., 2010. Colorimetric properties of reversible thermochromic printing inks. Dye. Pigment. 86, 271–277.

MacLaren, D.C., White, M.A., 2003. Dye-developer interactions in the crystal violet lactone-lauryl gallate binary system: implications for thermochromism. J. Mater. Chem. 13, 1695.

Phillips, G.K., 2000. Phillips SPIE 2000.pdf. In: Proceedings of SPIE. pp. 99–104.

Sage, I., 2011. Thermochromic liquid crystals. Liq. Cryst. 38, 1551–1561.

Seeboth, A., Lötzsch, D., 2008. Thermochromic Phenomena in Polymers. Smithers Rapra Technology Limited, Shropshire, UK.

Tang, H., MacLaren, D.C., White, M.A., 2010. New insights concerning the mechanism of reversible thermochromic mixtures. Can. J. Chem. 88, 1063–1070.

White, M., LeBlanc, M., 1999. Thermochromism in commercial products. J. Chem. Educ. 76, 3–7.

Worbin, L., 2010. Designing Dynamic Textile.

Zhu, C.F., Wu, A.B., 2005. Studies on the synthesis and thermochromic properties of crystal violet lactone and its reversible thermochromic complexes. Thermochim. Acta 425, 7–12.

This page was left blank intentionally!

Dynamic Load Balanced Clustering using Elitism based Random Immigrant Genetic Approach for Wireless Sensor Networks

K. Mohaideen Pitchai[1], B. Paramasivan[1], S. Anitha[1]

[1] Department of Computer Science and Engineering, National Engineering College, Kovilpatti–628503, Tamilnadu, India

Abstract

Wireless Sensor Network (WSN) consists of a large number of small sensors with restricted energy. Prolonged network lifespan, scalability, node mobility and load balancing are important needs for several WSN applications. Clustering the sensor nodes is an efficient technique to reach these goals. WSN have the characteristics of topology dynamics because of factors like energy conservation and node movement that leads to Dynamic Load Balanced Clustering Problem (DLBCP). In this paper, Elitism based Random Immigrant Genetic Approach (ERIGA) is proposed to solve DLBCP which adapts to topology dynamics. ERIGA uses the dynamic Genetic Algorithm (GA) components for solving the DLBCP. The performance of load balanced clustering process is enhanced with the help of this dynamic GA. As a result, the ERIGA achieves to elect suitable cluster heads which balances the network load and increases the lifespan of the network.

Keywords: Genetic Algorithm, Elitism, Load Balanced Clustering, Random Immigrants, Wireless Sensor Network

1. Introduction

In recent years, an energy efficient design of a Wireless Sensor Network (WSN) has become a leading area of research. WSN consists of base stations and numbers of nodes (wireless sensors). Energy efficiency is the essential criteria to increase the lifespan of the network. Clustering is the key technique used for load balancing to extend the lifetime of a sensor network by reducing energy consumption. Cluster structure can prolong the lifetime of the sensor network by making the cluster head aggregate information from the nodes in the cluster and send it to the base station.

The clustering concept offers tremendous benefits for WSN. The importance of the clustering problem can be summarized in two aspects. First, it plays an essential role in effective network management. The flat network infrastructure of WSN encounters the scalability problem when the network size keeps rising. In WSNs

node mobility, scalability is more challenging factor. Therefore, effective network management is extremely important. So far, clustering is the most efficient way to manage WSN. Second, clustering serves as the foundation for many other key problems in WSN (e.g., routing, intrusion detection, topology control, and backbone construction). All these problems are solved based on a well clustered network structure. In this paper, the load balance is used a clustering metric since it is a vital application requirement. It can guarantee the fairness for all the cluster heads in terms of the workload. Moreover, the load balanced clustering will prolong the lifespan of the cluster structure since every cluster head can evenly consume its battery energy.

The objective of this paper is to solve the Dynamic Load Balanced Clustering Problem (DLBCP) in WSN and also to maximize the

network lifetime and minimizes the network energy consumption. In this paper, a novel load balanced clustering approach using Genetic Algorithm (GA) is proposed. This proposed work forms clusters with optimal cluster heads. Here the genetic algorithm is applied along with the weighted clustering algorithm and this improves the performance of the network and also balances the load in the network.

2. Related work

Various works has been surveyed which provides solutions for the DLBCP problem. Some of the important works has been reviewed which are described as follows. Huicheng et al [1] formulates the DLBCP into a dynamic optimization problem. They proposed to use a series of dynamic Genetic Algorithms (GA) to solve the DLBCP in MANETs. In this dynamic GA, each individual represents a feasible clustering structure and its fitness is evaluated based on the load balance metric. Various dynamics handling techniques are introduced to help the population to deal with the topology changes and produce closely related solutions in good quality. Their experimental results show that these GA can work well for the DL-BCP and outperforms traditional GA that do not consider dynamic network optimization requirements. Xiaohui Yuan et al [2] proposed a genetic algorithm based, self-organizing network clustering (GASONeC) technique that has a framework to dynamically optimize wireless sensor node clusters. In GASONeC, the residual energy, the expected energy expenditure, the distance to the base station and the also the range of nodes in the vicinity are employed in search for a best, dynamic network structure. Reconciliation these factors is that the key of organizing nodes into applicable clusters and designating a surrogate node as cluster head. Here the authors contributed the work into two folds. First, a GA based clustering method is proposed that maintains the dynamic cluster structure. Second, it balances the energy consumption of every node and improves the network lifetime.

Kaliappan **e**t al [3] used energy metric in genetic algorithm (GA) to solve the DLBCP. They used genetic algorithms such as elitism based immigrants genetic algorithm (EIGA) and

memory enhanced genetic algorithm (MEGA) to solve DLBCP. These schemes select an optimal cluster head by considering the distance and energy parameters. They used EIGA to maintain the diversity level of the population and MEGA to store the old environments into the memory. It promises the load balancing in cluster structure to increase the lifetime of the network. Their experimental result shows that their proposed schemes increases the network lifetime and reduces the total energy consumption.

Vipin pal et al [4] presented a genetic algorithm based cluster head selection for centralized clustering algorithms to have a better load balanced network than the traditional clustering algorithm. Here the cluster head is selected according to their residual energy and takes care of trade-off of inter and intra cluster communication distance. Also their proposed scheme optimizes the number of cluster head for a round. Their simulation shows that their proposed solution finds the optimal cluster heads and has prolonged network lifetime than the traditional clustering algorithms.

Pratyay Kuila [5] proposed the load balanced clustering problem in WSN. In this paper, the author used the genetic algorithm approach to solve the load balancing problem in WSN. This proposed algorithm performs well for both equal as well as unequal load of the sensor nodes. The author performs in depth simulation of the proposed method and compares the results with some evolutionary based approaches and other related clustering algorithms. The results demonstrate that the proposed algorithm performs better than all such algorithms in terms of varied performance metrics like load balancing, execution time, energy consumption, number of active sensor nodes, and number of active cluster heads and also the rate of convergence.

Sheng Xiang Yang et al [6] proposed the random immigrants and memory scheme. The random immigrant scheme addresses dynamic environments by maintaining the population diversity while the memory scheme aims to adapt genetic algorithms quickly to new environments by reusing historical information. Experimental results show that the memory-based and elitism-based immigrant schemes

efficiently improve the performance of genetic algorithms in dynamic environments.

3. Dynamic Load Balanced Clustering Problem

The DLBCP problem is described as follows. For a given sensor nodes, the proposed algorithm is to find a set of cluster heads from the network and each cluster head serves the same number of cluster members. Due to some environmental changes the topology of the network also changes from time to time. Therefore the objective of this paper is to find suitable cluster heads in WSN with dynamic environment.

The proposed algorithm consists of various phases like genetic representation, population initialization, fitness function calculation, selection, crossover, and mutation. Initially the deployed sensor nodes are represented using genes. Then populations are generated using random permutation of chromosomes. In genetic algorithm, each chromosome represents a potential solution. In the next phase, the weight value of each node presented in a chromosome is calculated by using weighted clustering process [7,8]. Then the procedure for cluster head selection is applied to select suitable cluster heads from each chromosome. The calculated weight values for each node in the chromosome is used to find out the fitness value of that chromosome by taking the sum of weight values of all cluster heads in this particular chromosome. Next the selection operator is formulated to ensure that the better chromosomes of the population with higher fitness value have greater probability of being selected for mating. In order to achieve the same, roulette wheel selection method is used. Finally the important GA operations namely cross over and mutation is applied.

The crossover helps to select suitable best individual from current population and to produce the new population. Mutation alters one or more gene values in a chromosome from its initial state and the new gene values are added to the gene pool. From the new gene values the better solution may be obtained. As a result a new child chromosome is generated whose corresponding cluster head sets are the finalized cluster heads of the given network topology. Whenever the environment change s, the

network topology also changed which leads to change the cluster structure and also the cluster heads will be changed. Hence this proposed method uses the elitism based random immigrant method to adapt dynamic topology changes. Finally the load balanced cluster structure is obtained. Figure 1 shows the flowchart of the proposed ERIGA algorithm.

Fig.1 Flowchart of ERIGA Algorithm.

3.1 Genetic Representation

In WSN, the nodes which are presented initially are considered as population. It is denoted as

$$P = \{n_1, n_2, \ldots, n_m\} \quad (1)$$

Each node in the network has a node ID. Each node ID represents a gene. The random permutation of node IDs are used to represent a chromosome.

3.2 Population Initialization

The initial population is represented as P_{GA} and it consists of 'q' (=m!) chromosomes. It is denoted as

$$P = \{CHr_o, CHr_1, \ldots, CHr_{q-1}\} \quad (2)$$

In GA, each chromosome represents a potential solution. If 20 numbers of nodes are presented in a network then there are 20! Chromosomes can be obtained. It guarantees that each chromosome has no duplicate ID and it explores the population diversity for each chromosome. Hence a random set of cluster heads can be derived by using random permutation of node IDs.

3.3 Weighted Clustering

After the formation of the initial population, weight w_v of each node was calculated by using

weighted clustering procedure. Genetic algorithm uses those values to sum up for all the cluster heads for each chromosome. W_v is defined as

$$W_v = W_1\Delta_v + W_2 m_v \qquad (3)$$

Where Δ_v is the degree difference and m_v is the average speed of the nodes. The corresponding weighing factors are such that.

$$\sum_{i=1}^{2} W_i \qquad (4)$$

This procedure consists of the following steps.

1. Find the degree of each node d_v. It is defined as the number of neighbor nodes N(v). It can be calculated as

$$d_v = N(v) = \sum_{v' \in V, v' \neq v} (dist(v, v') < tx_{range}) \qquad (5)$$

Where tx_{range} is the transmission range of v and V represents the set of nodes v_i. The neighborhood of a cluster head is the set of nodes within its transmission range.

2. Degree difference (Δ_v) is one of the performance parameter for load balancing. It is defined as the difference of ideal node degree (δ) and actual degree (connectivity) of that node. Degree of node (d_v) is the number of neighbors of node v that are in the transmission range. Ideal degree is the number of neighbors that a cluster head can handle effectively. The degree difference for every node v can be calculated as

$$\Delta_v = |d_v - \delta| \qquad (6)$$

3. Mobility is an important factor to decide efficient cluster heads and it is used to avoid frequent cluster head changes. It is computed using the average running speed for every node till the current time T. The mobility of a node m_v is calculated as

$$m_v = (1/T) \cdot \sum_{t=1}^{T} \sqrt{(x_t - x_{t-1})^2 + (y_t - y_{t-1})^2} \qquad (7)$$

Where (x_t, y_t) and (x_{t-1}, y_{t-1}) are the coordinates of node v at time t and t-1 respectively.

4. Weighing factors are chosen in such a way that $w_1 + w_2 = 1$. Calculate the combined weight w_v for each node v, where

$$w_v = w_1\Delta_v + w_2 m_v \qquad (8)$$

where w_1 and w_2 are weighting factors. Repeat the steps 2-4 for remaining nodes.

3.4   An illustrative scenario

Consider a network consists of 20 nodes with IDs ranging from 0 to 19. The transmission range for each node is represented by a circle with equal to radius. The weighted clustering algorithm is demonstrated with figures 2 to 6. Figure 2 shows that the initial configuration of 20 nodes with node IDs
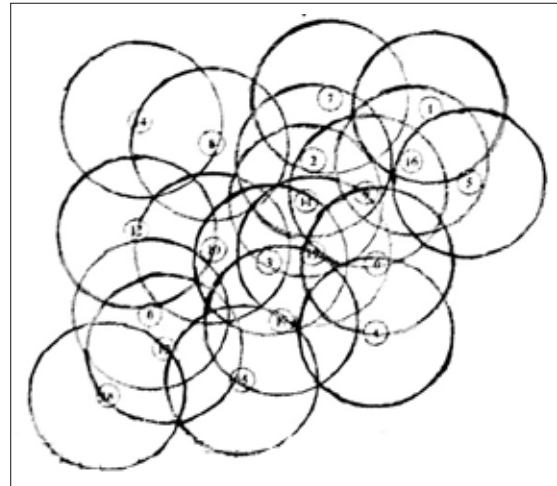

Fig.2. Initial configuration consists of 20 nodes.

Figure 3 shows the neighbors of each node. The neighbors of the each node v are defined by its degree d_v. Step 1 implies that degree, d_v, which is the total number of neighbors of a node. The degree difference, Δ_v, of each node is calculated in step 2 with ideal node degree $\delta=2$. The mobility of node is calculated in step 3 and the m_v values are chosen randomly. If $m_v=0$ means the node does not move ie static node.
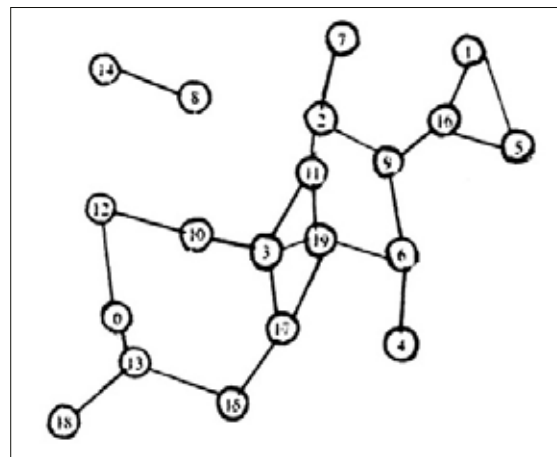

Fig.3. Neighbors identified for each node.

In Figure 4, the arrows indicate the speed and direction of movement of every node. The weighted metric w_v for each node is computed

Dynamic Load Balanced Clustering using Elitism based Random Immigrant Genetic Approach for Wireless Sensor Networks

in step 4. The values of weights are considered as w_1=0.5 and w_2=0.5. So these weighting factors are chosen randomly according to w_1+w_2=1.
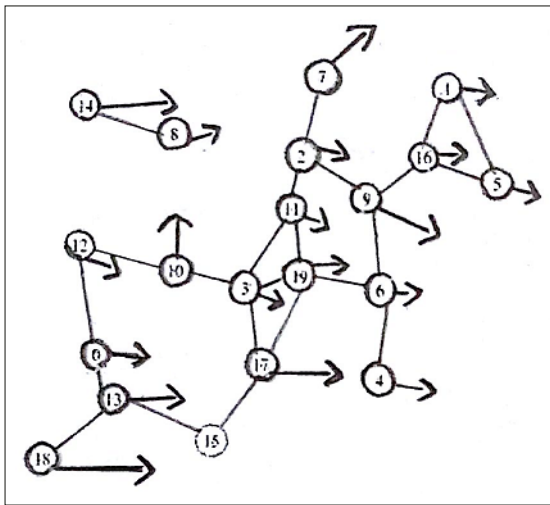

Fig.4. Mobility of the nodes.

Table 1 represents the execution of weighted clustering algorithm. The cluster head results are shown in the form of table. The first column in the table represents the node ID. The values in the second column of the table represent the degree of the each node and the degree difference values are represented in third column of the table. The randomly chosen mobility values are represented in fourth column of the table. Finally the fifth column shows the weighted values of each node.

Table 1. Execution of weighted clustering

NODE ID	d_v	Δ_v	m_v	w_v
0	2	0	2	1
1	2	0	1	0.5
2	3	1	1	1
3	4	2	1	1.5
4	1	1	2	1.5
5	2	0	1	0.5
6	3	1	1	1
7	1	1	2	1.5
8	1	1	1	1
9	3	1	3	2
10	2	0	2	1
11	3	1	1	1
12	2	0	1	0.5
13	3	1	2	1.5
14	1	1	3	2
15	2	0	0	0
16	3	1	1	1
17	3	1	3	2
18	1	1	4	2.5
19	4	2	1	1.5

This is stored in a list where each node is pointing to its neighbor's list as it is next position that is used to compute the object function. Table 2 represents the neighbor lists of each node.

Table 2. Neighbor list of each node

w_v values	Node id of all nodes	Neighbor's list
1	0	→ 12 → 13 →
0.5	1	→ 5 → 16→
1	2	→ 7 → 11 →
1.5	3	→17 → 10 →11 → 19
1.5	4	→ 6 →
0.5	5	→16 → 1 →
1	6	→ 4 → 19 → 9
1.5	7	→ 2 →
1	8	→ 14→
2	9	→ 2 → 16 → 6→
1	10	→ 3 → 12 →
1	11	→ 2 → 3 →19 →
0.5	12	→0 → 10 →
1.5	13	→0 →18 → 15 →
2	14	→ 8 →
0	15	→13 → 17 →
1	16	→ 9 → 1 → 5 →
2	17	→ 3→ 15 → 19 →
2.5	18	→ 13 →
1.5	19	→11 → 6→17→ 3 →

3.5 Cluster Head Selection

The algorithm goes through each node in this list and checks three conditions in order to select the current node as a cluster head.

1. If the node under consideration is not already a cluster head.
2. The node is not a member of any cluster heads.
3. The actual number of neighbor is less than threshold value (T=4).

If these three conditions are satisfied, then the nodes are selected as a cluster heads and inserted into the set of cluster heads for that particular chromosome. The selected cluster heads are shown in the figure 5.
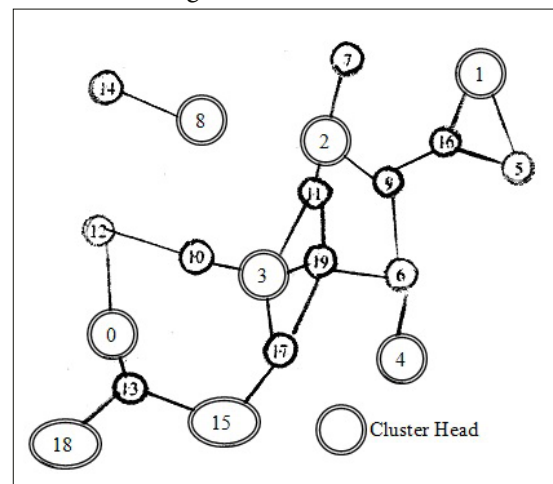

Fig. 5. Cluster heads selection

Table 3. Cluster heads set for a single chromosome.

w_v values	Node id of all nodes	Neighbor's list
1	0	→12 → 13 →
0.5	1	→ 5 → 16→
1	2	→ 7 → 11 →
1.5	3	→ 17→ 10 →11 →19 →
1.5	4	→ 6 →
1	8	→ 14 →
0	15	→ 13 →17 →
2.5	18	→ 13 →

3.6 Fitness Function Calculation

After the cluster heads are chosen, the calculated w_v values for each node is used to find out the fitness value of the chromosome by taking the summation of w_v values of all cluster heads in this particular chromosome. Since the orders of appearance of node IDs of the chromosome are different, each chromosome will have a different set of cluster heads which in return will have the different fitness value. This fitness function is used to estimate the quality of the chromosome. The fitness function of this chromosome is 9. So for each chromosome the fitness function is calculated and after that it chooses the highest fitness value chromosomes. These fitness chromosomes are then served as parents for the next generation.

3.7 Selection

Selection plays a vital role in improving the average quality of the population by passing the prime quality chromosome to the next generation. The selection operator is formulated to ensure that better chromosomes of the population with higher fitness vale have greater probability of being selected for mating. Roulette Wheel selection is used to select individuals based on their fitness values. Therefore the probability of choosing an individual depends directly on its fitness value. This probability is defined as

$$P_i = \frac{F_i}{\sum_{j=1}^{n} F_j} \qquad (9)$$

where F_i and n are the fitness chromosome and size of the population respectively. The size of each individual corresponds to fitness value of associated individuals. The circumference of the roulette wheel is the sum of all fitness values of individuals. The fittest chromosome occupies the largest interval, whereas the least fit has small interval within the roulette wheel. In this method, circular wheel is divided and a fixed point is chosen on the wheel circumference and the wheel is rotated. The region of the wheel which comes in front of the fixed point is chosen as the parent and for the second parent same process is repeated. Two individuals are then chosen randomly based on the probabilities and produces offspring.

3.8 Crossover

Crossover is a genetic operator that mixes two chromosomes to provide a new Chromosome. The crossover is used to choose the new chromosome that may be better than both of the parents, if it takes the best characteristics from each of the parents. They help to select suitable best individual from current population and to produce the new population. Here order 1 crossover method is used. In this method, initially selects two parent chromosomes and calculate the residual energy for all the nodes and then arrange the parent chromosomes by value of residual energy (i.e.) from high remaining energy to low remaining energy and then selects a random swath of consecutive gene from two parent chromosomes. After that from parent chromosome 1 and it drops the swath down to child 1 and remaining genes are taken from the second parent chromosome. From the second parent chromosome starting on the right side of the swath, grab genes from parent 2 and then insert them in child 1 at the right edge of the swath. This procedure is repeated for the second child chromosome. For the second child chromosome swap area is selected from the parent chromosome and then remaining genes are genes are grabbing from the parent chromosome 1. Figure 6 shows the illustration of the crossover.
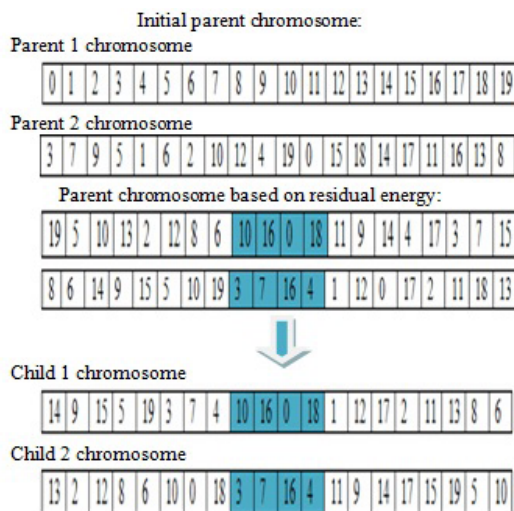
Fig. 6. Illustration of crossover.

3.9 Mutation

Mutation is a genetic operator used to preserve genetic diversity from one generation of a population of a chromosome to the consequent generation. Mutation alters one or more gene values in a chromosome from its initial state and the new gene values are added to the gene pool. From the new gene values the better solution may be able to obtain. Here gene swapping method is used for generating a children chromosome from a parent chromosome by changing the value of some genes.

In Mutation, initially the residual energy for all the nodes are calculated and selects a parent chromosomes and then arrange the parent chromosome by value of residual energy (i.e.) from high remaining energy to low remaining energy. Then selects two positions on the chromosome at random, and interchanges the values. This is common in permutation based encodings. In the example, genes 9 and 0 are swapped and this is shown in the figure 7.
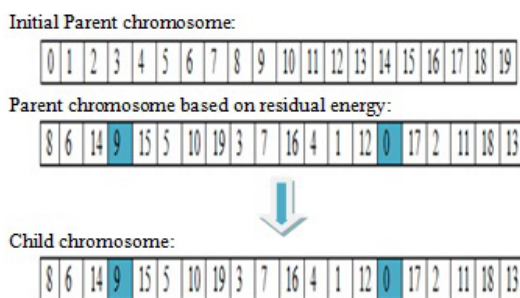

Fig.7. Illustration of mutation

As a result of mutation, a new child chromosome is generated whose corresponding cluster head sets are the finalized cluster heads of the given network topology. This procedure is repeated until the new population is equal to the initial population. These are the standard genetic algorithm operations. If the topology changes, then the dynamic genetic operations such as immigrant schemes or memory based schemes can be used. This proposed method uses the elitism based random immigrant approach for the dynamic load balanced clustering problem.

3.10 Elitism based Random Immigrant Approach

Standard genetic algorithm is not suite well for the dynamic environments. If the load balanced clustering problem is considered in a dynamic environment, then it is termed as dynamic optimization problem. There are various methods are used to solve dynamic optimization problem. The best method is to enhance the performance of the dynamic optimization problem through immigrant schemes. The basic idea behind the immigrant scheme is to introduce new individuals into the current population by replacing the worst individuals. It can remove the diversity level of the population. The above said conventional genetic operations are combined with immigrant schemes to solve dynamic load balanced clustering problem.

Here an elitism based random immigrant approach is used. After the crossover and mutation operations, every chromosome is evaluated and checks their fitness value. Due to some environment conditions, the network structure may change and that affects the fitness value of the chromosomes (i.e.) if the topology changes then the cluster structure are changed and also their corresponding cluster heads will changed. The fitness value is calculated based on the cluster heads of each chromosome. So the fitness value is affected after the environment changes. So this affects the current population and for that this work uses the Elitism based Random Immigrant Genetic Algorithmic approach (ERIGA).

In ERIGA, new immigrants which include the random and elite immigrants are generated first and then they replace the worst individual

in the current population. The random immigrants are feasible solutions generated randomly which aims to increase the diversity level of the population. The elite immigrants are used to reserve the better individuals in current generation to the next generation. From the previous generation, the chromosomes with the higher fitness value (elites) are stored and this elites can use for the replacement strategy.

After the execution of standard GA operations, the current population is evaluated. If the chromosome with the least fitness value is found, then it is replaced with the higher fitness value chromosomes from the previous generation and then performs the standard genetic operations. Finally update the current generation with new individuals. This process is repeated until the maximum population is reached. The pseudo-code for the ERIGA is shown below.

Algorithm ERIGA
Evaluate the current population
//Perform elitism based immigrant mechanism
Generate elite immigrant from p(t-1)
Evaluate elite immigrants
// (i.e. immigrant with high fitness value)
If environment change is detected
Then
Replace the worst individual (i.e. individual with low fitness value) in p (t) with generated immigrant from p(t-1)
Else
Perform basic genetic operations
Update population until the termination criteria is met
End

---

4. Simulation and Results

The simulation experiments are conducted to evaluate the performance of the proposed ERIGA algorithm for the concerned Dynamic load balanced clustering problem. Simulation has been carried out using MATLAB tool. The simulation parameter settings are tabulated in Table 4. The EIRGA algorithm is executed by considering an initial population of 100 chromosomes. For crossover operation, ERIGA selects the best 10% chromosomes using Roulette Wheel selection. The crossover rate is taken as 0.6 and mutation rate as 0.03. The algorithm is run for 20 iterations. The ERIGA algorithm is compared with Standard GA (SGA) algorithm.

Table 4. Simulation Parameters Settings

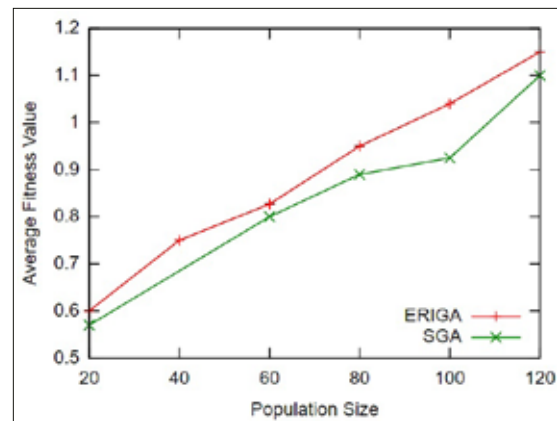| Parameter	Value/Method
Deployment Area	100 x 100 m²
Base Station Location	(50,50)
Network Size	20-100
Initial Energy of Nodes	0.5J
Population Initialization	Random
Number of Generations	10-100
Selection Schema	Roulette Wheel Selection(RWS)
Cross Over Rate	0.6
Mutation Rate	0.03
Replacement Rate	0.1-0.6
Selection Ratio of Random Immigrants	0.2
Selection Ratio of Elite Immigrants	0.4

Fig. 8. Population Size Vs Average Fitness Value.

Figure 8 shows the comparison of average fitness value with SGA and ERIGA. The average fitness value is increased by increasing the size of the population. During the population size of 100, the average fitness value of SGA is 0.9. But in the case of ERIGA, the value is 1.1. This is due to the replacement of worst individuals in the identified chromosome with elite chromosomes. When the replacement rate is increased, the difference of average fitness value will be increased.

Figure 9 shows the comparision among number of cluster heads with the varying size of population. It is observed that during the population size of 60 and 80, the number of cluster head of ERIGA is 12 and 11. This variation is due to the variation in mobility speed of the nodes. There is a linear increase in the number of cluster heads after the population size is varied from 80 to 140. It is also observed that during the population size of 60, both SGA and ERIGA has same number of cluster heads. In
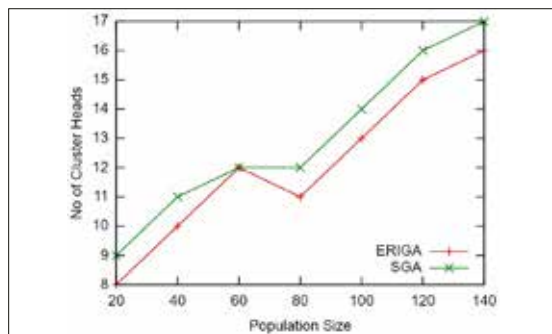
that scenario, there is no mobilty is considered in ERIGA.

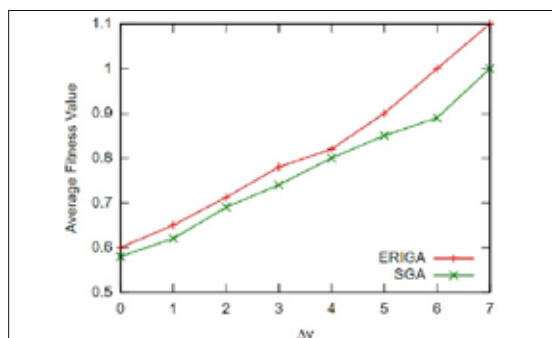**Fig. 9. Population Size Vs Number of Cluster Heads**

Fig. 10. Average Fitness Value by varying the value of Δ_v

Figure 10 shows that the average fitness value of ERIGA and SGA for different values of Δ_v. In ERIGA, the average fitness value varies from 0.6 to 1.1 and for SGA it varies from 0.55 to 1. When the value of Δ_v is 6, the average fitness value of ERIGA and SGA are 1 and 0.85 respectively. The degree difference Δ_v value is due to the mobility consideration. Hence the ERIGA achieves highest fitness value as compared with SGA. Also whenever a Δ_v value varies, the corresponding W_v values are varied and thus it changes the fitness value of that particular chromosome.
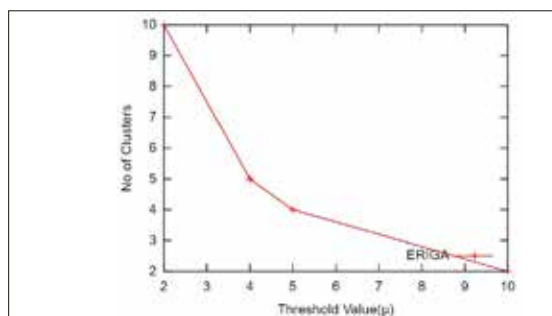

Fig. 11. Threshold Value Vs Number of clusters

Figure 11 shows that the number of clusters formed based on the threshold values for a

network of size 20 nodes. Here the threshold value is set to 4. The threshold value represents the number of members within a cluster. According to that number of clusters is formed corresponding to the threshold values.
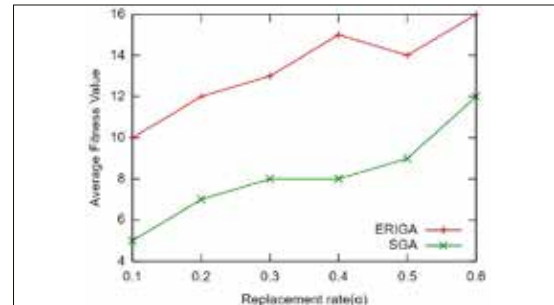

Fig. 12. Replacement Rate Vs Average Fitness Value

Figure 12 depicts that the average fitness value of ERIGA and SGA with different values of replacement rate. Replacement rate is defined as how much of chromosomes in the current generation are replaced with the previous generation. When the replacement rate is 0.4, the average fitness value of SGA is 8. But this value is increased up to 15 for ERIGA. Since the replacement of worst individuals in the previous generation with elites in the current generation. These results will improve the performance of the proposed ERIGA algorithm.

5. Conclusion

The characteristic such as topology dynamics due to energy conservation and node movement in WSN leads to dynamic load balanced clustering problem. Load balancing and reliable information transfers among all the nodes are essential to prolong the lifespan of the network. In this paper, genetic algorithm is used to solve the dynamic load balanced clustering problem. Initially a standard genetic approach was applied to solve the load balanced clustering problem. In order to adapt a dynamic environment, the standard approach is enhanced to a dynamic genetic algorithmic approach called elitism based random immigrant approach. This is applied to find suitable cluster heads whenever topology changes. The simulation results show that the dynamic approach is more suitable than a static method to solve the dynamic load balanced clustering problem. In future, heterogeneous WSN may be considered

for testing the applicability of the proposed load balanced algorithms SGA and ERIGA.

References

[1] Hui Cheng, Sheng Xiang Yang and Jiannong Cao, "Dynamic genetic algorithms for the dynamic load balanced clustering problem in mobile ad hoc networks", Journal of Expert Systems with Applications, Elsevier Publications, Vol.40, pp.1381-1392, 2013.

[2] Xiaohui Yuan, Mohamed Elhoseny, Hamdy K El-Minir and Alaa M. Riad, "A genetic algorithm based dynamic clustering method towards improved WSN longevity", Journal of Network and System Management, Springer Publications, Vol.24, pp.1-26, 2016.

[3] Kaliappan, Mariappan, Viju Prakash and Paramasivan, "Load Balanced Clustering Technique in MANET using Genetic Algorithms", Defence Science Journal, Vol. 66, No. 3, pp. 251-258, 2016.

[4] Pratyay kuila, Suneet K Gupta and Prasanta K Jana "A novel evolutionary approach for load balanced cluster problem for wireless sensor networks", Journal of Swarm and Evolutionary Computation, Vol.12, pp.48-56, 2013.

[5] Sheng Xiang Yang, "Genetic Algorithms with Memory and Elitism based Immigrants in Dynamic Environments", Journal of Evolutionary Computation, Vol. 16(3), pp.385–416, 2008.

[6] Dipak Wajgi, Nilesh Singh, "Load balancing based approach to improve lifetime of wireless sensor network", International Journal of Wireless & Mobile Networks, Vol. 4, No. 4, pp.155-167, 2012.

[7] Vaibhav Deshpande, Arvind Bhagat Patil, "Clustering for improving lifetime of wireless sensor network: A Survey", International Journal of Engineering Science Invention, Vol. 2, pp.1-6, 2013.

[8] Mainak Chatterjee, Sajal Das and Damla Turgut, "WCA: A Weighted Clustering Algorithm for Mobile Ad Hoc Networks", Journal of Cluster Computing, Vol.5, No.2, pp.193–204, 2002.

Degradation of inkjet ink by greensand and ultrasonic sonification

Mirela Rožić[1], Marina Vukoje[1], Kristinka Vinković[2], Nives Galić[2], Mirela Jukić[3]

[1] University of Zagreb Faculty of Graphic Arts, Getaldićeva 2, Zagreb, Croatia

[2] University of Zagreb Faculty of Science, Department of Chemistry, Horvatovac 102a, Zagreb, Croatia

[3] Andrija Stampar Teaching Institute of Public Health, Mirogojska 16, Zagreb, Croatia

Abstract

The study describes the degradation of inkjet ink at low frequency ultrasound (US) and greensand to compare their reactivity. Environmental sonochemistry is a rapidly growing area and an example of the advanced oxidation process (AOP) that deals with the destruction of organic species in aqueous solutions. Greensand is a granular material coated with a thin layer of manganese dioxide (MnO_2) which is among the strongest natural oxidants. In our study magenta inkjet water-based printing ink was dissolved in distilled water and the solutions obtained after degradation were analysed in terms of total organic compound (TOC) and absorption curves in the visible spectra. Also used for the process monitoring was high performance liquid chromatography (HPLC). The efficiency of discoloration is significantly affected by the effluent pH. The efficiency of discolouration was higher when the pH of initial solution was 2 with respect to the initial solution pH of 5.5. In all solutions, irrespective of the initial pH value and the processing method the oxidation of polyhydric alcohols occurs. Although the decomposition is significant, surface peaks resulting from HPLC analysis are very small. Decolourization is closely related to the cleavage of the – C=C and -N=N- bonds, and oxidation of polyhydric alcohol to the formation of monosaccharides, carboxylic acids or other low molecular weight compounds with a lesser number of unsaturated double bonds. These compounds have low UV absorbance or they absorb below 200 nm and therefore their detection is impossible. Thus, the obtained total organic compound results indicate a small degree of mineralization. The effectiveness of the low-frequency ultrasound (20 kHz) oxidation is similar to the effectiveness of oxidation by greendsand.

Key words: oxidiation, ultrasound, greensand, inkjet printing ink

1. Introduction

Wastewater effluents in some industries, such as dyestuff, textiles, leather, paper, and plastics contain several kinds of synthetic dyestuffs. The presence of colour in water for whatever use is undesirable (Guzman-Duque et al., 2011). Even with the presence of very small amounts of dyes in water (less than 1mg dm^{-3} for some dyes) the colour is highly visible (Wu et al., 2013) and can be toxic for life and harmful for human beings. Hence, the removal of colour from process or waste effluents is an issue of fundamental importance for the environment (Mohamed et al., 2007, Wu et al., 2013, Vončina Brodnjak and Majcen-Le-Marechal, 2003).

Until now, conventional methods such as coagulation, microbial degradation, absorption on activated carbon, incineration, biosorption, filtration, and sedimentation have been used to treat dye wastewater. During the last two decades, Advanced Oxidation Processes (AOPs) have emerged as sludge-free alternatives for decolourizing azo dyes (Eren and Ince, 2010). Ultrasound is considered to be an advanced oxidation process (AOP) that generates OH• radicals through acoustic cavitation (Eren, 2012). The sonochemical effect takes place at the gase/liquid interface due to the oxidation of organic molecules by OH• and, to a lesser extent, in the bulk solution or the pyrolytic decomposition inside the bubbles. Hydrophilic and non-volatile compounds such as dyes mainly degrade through OH-mediated reactions in the bulk solution and at the bubble-liquid interface, while hydrophobic and volatile species degrade

thermally inside the bubbles (Eren, 2012; Moumeni et al., 2012).

Researchers have shown that high frequencies are usually effective in degrading hydrophilic and non-volatile organics such as dyes, while low frequencies are more suitable for hydrophobic and volatile compounds. The result was attributed to a larger number of oscillations at high frequency that allowed a larger fraction of OH-ejection into the bulk liquid (Rehorek, 2004; Eren, 2012; Eren and Ince, 2010).

According to Guzman-Duque et al. (2011) by-products of aromatic structures occured as a result of sonochemical degradation of crystal violet dye in water. As demonstrated by Siddique et al. (2011) sonoelectrochemical treatment of un-hydrolyzed reactive blue 19 dye for 30 min resulted in the formation of acetic acid, benzoic acid, etc. For hydrolyzed dye, a treatment of 10 min was enough. According to Moumeni et al. (2012) sonochemical degradation of malachite green occurs via two competitive processes: N-demethylation and destruction of the conjugated structure.

Greensand is a granular material, coloured in purple-black, derived from glauconite. Glauconite is a very common mineral in the class of zeolite, coated with a thin layer of manganese dioxide (MnO_2). Manganese oxides are among the strongest natural oxidants in soils and sediments with a reducing potential between 1.27 and 1.50 V. They are capable of oxidizing many inorganic pollutants and a wide range of organic compounds such as phenols, aromatic amines, antibiotics, alcohol and colorants (Wang et al., 2014; Markovski et al., 2014; Zhang et al., 2013; Hao et al., 2013; Clarkea et al., 2013; Qu et al., 2014; Zhua et al., 2010; Wang et al., 2017; Jiang et al., 2016; Das and Bhattacharyya, 2014; Fang et al., 2016; Dang et al., 2016).

Every inkjet formulation contains ingredients to preserve the colorant in a wet, fluid medium, whether solvent or carrier. Thus, water as a neutral fluid adjusts viscosity, adds volume, and allows the regulation of the concentration of the dye formulation. Then we have the surfactant and acid or alkali (base) to control the pH of the formulation (Cie, 2015). Water-based inkjet printing inks are comprised of colourant (dye or pigment), additives, humectants (ethylene glycol, polyethylene glycol, triethylene glycol or diethanolamine) and water. Originally coloured liquids (dye-based colourants) are fully dispersed and dissolved in water (Aldib, 2015).

About 50% of the dyes produced in the world are derived from azo compounds. The main characteristic of this family of compounds is the presence of the azo group (−N=N−), which allows larger extension of π-electronic conjugation and, therefore, intense absorption of light in the visible region of the electromagnetic spectrum (Ferreira, 2013). In water-based ink jet printing inks the anionic dyes are mostly used as colourants (Ferreira, 2013). Azo dyes themselves are not toxic. Under anaerobic conditions azo dyes are cleaved by microorganisms to form potentially carcinogenic aromatic amines. Aromatic amine formation may be avoided by the use of oxidative processes (Rehorek et al., 2004).

The oxidation of a mono-component system is the subject-matter of research of most of the authors of this paper. Thus, the oxidation of the real system, which consists of different organic components is presented. We studied the degradation of the components from a solution obtained by dissolving an inkjet water-based printing ink (dye-based) in distilled water. The oxidation process was conducted with greensand batch process and ultrasonic irradiation (low frequency ultrasound). The comparison of the effectiveness of the presented oxidation processes was given.

2. Material and methods

2.1 Model solution

Dye solution with a concentration of 100 mg dm^{-3} was prepared by dissolving of the magenta inkjet printing ink (Epson Stylus Pro 7000) in distilled water. According to the producer, the approximate composition of printing ink is as follows: 1.5% dye; 8% glycerol ($OHCH_2CH(OH)CH_2OH$), 28% ethilenglycol $[(CH_2)_2(OH)_2]$, 1% urea and 61.5% water.

2.2 Chemicals

The chemicals used have the purity of the corresponding analytical grade from producer "Kemika" Zagreb. Distilled water with the electrical conductivity of less than 1 mS cm^{-1} was also used. For adjusting the dyestuffs' pH value

to 2.0 H_2SO_4 solution the concentration of 2 mol dm^{-3} was used.

2.3 Apparatus

Total organic carbon analyzer, (TOC-V$_{CHN/CSN}$, Shimadzu Corporation, Japan) was used for TOC concentration measurements. pH value was measured using inoLab_IDS, Multi 9310. Dyestuff model solutions were mixed using the rotary shaker Edmund Bűhler GmbH. Ultraconisc sonification was conducted using Sonopuls HD 3100 ultrasound with frequency of 20 kHz. The spectral absorption curves were determinated with Konica Minolta Spectrophotometer CM-3600d. UV–Vis spectrometry was performed with a Perkin Elmer, Lambda 10 spectrophotometer. The spectra were recorded between 200 and 800 nm at a scan rate of 240 nm min^{-1}.

The HPLC analyses were carried out on Agilent 1100 Series system consisting of quaternary pump, vacuum degasser, autosampler, thermostated column oven and multichannel UV diode-array detector (Agilent Technologies, Palo Alto, CA, USA). Chromatographic separation was carried out on a Zorbax Eclipse XDB column (150 mm × 4.6 mm) with C$_{18}$ functional groups and 5 µm particle size (Agilent Technologies, Palo Alto, CA, USA). The column temperature was 40 °C, injection volume 50 µL, flow rate of the mobile phase 1 mL min^{-1}, and the time of analysis 43 min. The mobile phases A (0.34 g TBASH + 900 mL water + 100 mL acetonitrile) and B (acetonitrile) were used for gradient elution as follows: the initial ratio of 25 % of acetonitrile was held constant for 5 min, then the ratio of acetonitrile was increased to 40 % over the following 8 min, and to 90 % in the following 17 min, held constant for 10 min and decreased to the initial value of 25 % over 0.5 min. The analytes were detected by monitoring the UV absorbance at 204 nm, 238 nm, 287 nm and 538 nm, which were set according to the UV absorption spectra of the initial sample solution.

2.4. Analitical procedure

2.4.1 Greensand oxidation treatment

Experiments were conducted in batch reactors at 25ºC. 0.25 g of greensand was placed into the plastic laboratory containers (50 cm^3) and covered with 25 cm^3 dyestuff soultion. The soultion was shaken on rotary shaker at a speed of 250 rotation/min during 10, 30, 60 and 220 min.

2.4.2. Ultrasonic oxidation treatment

25 cm^3 of dyestuff solution was placed into the laboratory beakers. The power of ultrasound was adjusted to 30, 80 and 150 W. Duration of treatment was 10, 20 and 30 min.

After treatments, all the soultions were centrifugated and in the obtained supernatants the TOC was determined and the absorption spectra were acquired in the visible spectral range. The HPLC analyses were used to monitor the initial and degradation products visible by the UV-VIS absorption detection. 50 µL of each sample was injected on the column, without any preparation or dilution.

3. Results and discussion

3.1 Oxidation by greensand

Figure 1 presents the TOC concentration measurements in original dyestuff solution and in all soultions treated with greensand. The initial pH values of dyestuff solutions were 5.5 and 2.0.

Fig.1.

After 10 minutes of treatment, the TOC concentrations were lower but this is negligible, as well as the further reduction which appeared with the increase of shaking time. The original dyestuff soultion has TOC concentration of 20 mg dm^{-3}. After 220 min of shaking, the TOC concentration in dyestuff solution with pH value 5.5 decreased to 15.87 mg dm^{-3}. The efficiency of TOC removal was around 20%. The soultion was slightly less coloured compared to original soultion but complete discolouration didn't occur. The removal of TOC in dystuff soultion with initial pH value of 2.0 is

approximately the same as in the initial dye-stuff solution with a pH value of 5.5. However, in acidic solutions discolouration has occurred (Figure 2).

Fig.2.

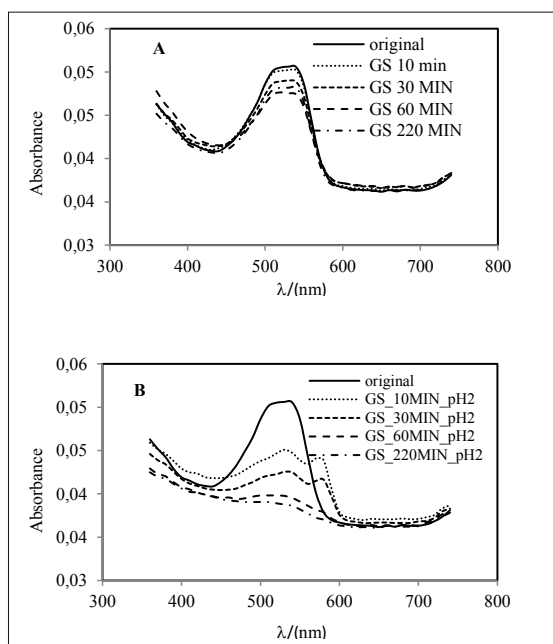Figure 2 shows the absorption spectra of dye-stuff soultions. A slight reduction of the absorption maximum of the initial solution with pH 5.5 (Figure 2A) and a significant reduction

of the absorption maximum in acidic solutions (Figure 2B) were observed.

Table 1 shows the recording wavelengths and retention times of 19 components monitored by the HPLC analysis.

The chromatograms of the initial solution recorded at 204 and 538 nm are shown in Figure 3. The peak with the retention time of 11.9 minutes represents the colour which is verified by recording its UV spectra during HPLC analysis using the diode array detector.

Fig.3.

Table 1

Peak No.		t_R / (min)	λ_{max} / (nm) wavelength of maximum absorption obtained from the recorded spectra	λ_{max} / (nm) wavelength at which a certain peak was recorded, i.e. in which the determined peak area was used in the results
1	A	1.3	204, 310	204
2	D	2.05	204	204
3	D	3.1	220, 250, 330	204
4	I	3.8	230, 275, 530	204
5	I	4.7	204, 230, 300	204
6	I (dye)	11.9	220-230, 280, 510-545	204
7	D	16.4	204	204
8	D	23.5	204	204
9	D	24.5	204, 230, 280	287
10	I	25.4	240-250	238
11	I	26.6	204, 230, 275	204
12	I	27.1	230	238
13	I	27.7	240, 250, 320, 345	238
14	I	28.5	280	287
15	I	29.1	204	204
16	I	29.6	204, 240, 305,	204
17	I	31.6	204, 300	204
18	I	35.6	204, 225, 260	204
19	I	38.8	204, 230, 275	204

Chromatogram of the initial solution contained 13 peaks recorded at different wavelengths. The components with the retention times of 2.05 min, 3.1 min, 16.4 min, 23.5 min i 24.5 min (peaks # 2, 3, 7, 8 and 9) were not detected in the initial sample solutions, but only in the solutions after treatment, so these components might be considered as degradation products (Table 1). A peak with the retention time of 1.3 min which is not present in the initial sample solution appears only in the acidified solutions, and probably relates to the sulphuric acid (Table 1). Other peaks belong to other components in the solution (alcohols). Two components with retention times of 35.5 and 38.7 minutes (peaks # 18 and 19) have significantly higher peak areas than the other peaks. These are probably the prevalent components in the samples (or the components with significantly higher UV absorbance than all other components). The components with the retention times of 4.7 min, 26.5 min, 29.1 min, 29.5 and 31.5 min (peaks # 5, 11 and 15-17) have lower peak areas than the previous two, but still significant and probably related to less concentrated compounds in the samples. The areas of the compounds with the retention times of 3.8 min, 25.4 min, 27.1 min, 27.7 min and 28.5 min are much lower than all the other peaks. These probably appertain to compounds with very low concentration or UV-VIS absorption (peaks # 4, 10, 12, 13, 14).

The surface areas of all the peaks that appear in the original dyestuff solution are reduced upon treatment with greendsand (Table 2) regardless to the initial pH value of solution except for peak # 6 (dye).

Table 2

Peak No.		Retention time/(min)	Peaks surface areas			
			Original dyestuff	30 min pH 5.5	10 min pH 2	20 min pH 2
1	A	1.3	0	0	238.9	216
2	D	2.05	0	0	113.9	123
3	D	3.1	0	0	68.5	55.7
4	I	3.8	26.5	0	20.5	25.9
5	I	4.7	649	45.5	168.6	157.6
6	I (dye)	11.9	115.6	136.4	0	0
7	D	16.4	0	0	60.8	74
8	D	23.5	0	324.5	326.1	327.7
9	D	24.5	0	31.8	31.4	31.9
10	I	25.4	137.1	54.1	53.6	54.9
11	I	26.5	1162	286.3	308.5	365.8
12	I	27.1	60.5	27.2	27.4	27.9
13	I	27.7	60.9	25.4	25.6	26
14	I	28.5	292	108.6	108.8	110.5
15	I	29.1	862.2	215.1	216.3	218.4
16	I	29.5	931.7	52.7	53.6	54.5
17	I	31.5	891.2	128.7	134.1	132.2
18	I	35.5	5705.5	2472.6	2494.4	2507.2
19	I	38.7	3054.2	1146.6	1155.3	1159.5

Area of peak # 6 is not reduced in a solution of pH 5.5, which means that there is no degradation of dyes. These results confirm the resulting absorption curve. Moreover, surface area of this peak is slightly higher. The total area of all peaks obtained by HPLC analysis of the original dyestuff solution is 13948.4. After greensand oxidation treatment of the original dyestuff solution (pH = 5.5) for 30 minutes, the total peak area is reduced to 4699.2. This means that the concentration of components in the solution has decreased by 66.3%. The surface area of resulting peaks was 356.3 representing only 2.5% of the initial surface. The greatest reduction of the peak surface areas was obtained for the peaks #5, 11, 15-17 in the neutral solution as well as for acid solution (from 75 to approximately 95% compared to the initial surface area of individual peaks, Table 3).

Table 3

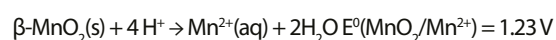| Peak No.		Retention time/(min)	% of degradation		
			30 min pH 5.5	10 min pH 2	20 min pH 2
4	I	3.8	100.0	22.6	2.3
5	I	4.7	93.0	74.0	75.7
6	I (dye)	11.9	-18.0	100.0	100.0
10	I	25.4	60.5	60.9	60.0
11	I	26.5	75.4	73.5	68.5
12	I	27.1	55.0	54.7	53.9
13	I	27.7	58.3	58.0	57.3
14	I	28.5	62.8	62.7	62.2
15	I	29.1	75.1	74.9	74.7
16	I	29.5	94.3	94.2	94.2
17	I	31.5	85.6	85.0	85.2
18	I	35.5	56.7	56.3	56.1
19	I	38.7	62.5	62.2	62.0

Other components are degraded in smaller percentage (from about 55 to 63%). Following the treatment of the acidic dyestuff solution with greensand for 10 minutes, the total surface area of the peaks obtained by HPLC analysis of the original dyestuff solution has decreased to 4766.7. The surface area reduction is 65.8%. The resulting surface is around 600.7.

After treatment of the acidic dyestuff solution with greensand for 20 minutes, the total surface area of the peaks present in the original dyestuff solution has decreased to 4840.4. The surface area reduction is 65.3%. The resulting surface is around 538.3. Slightly larger resulting surface areas of the peaks in the acidic dyestuff solution can be attributed to the decomposition of dyes and production of its degradation products (peaks #2, 3 and 7; Table 2). Although the decomposition is significant and most likely outlines the alcohol degradation, resulting surface peaks are very small.

However, it is possible that during degradation of these components the formed products of decompositions at the tested wavelengths have little or no absorbance and therefore their detection is impossible. HPLC analysis results of the dyestuff solution after shaking with the greensand (Table 2) did not differ significantly. Based on the obtained TOC results, we can assume that there was a slight mineralization.

Monosaccharides and carboxylic acid are formed by oxidation of polyhydric alcohols. Monosaccharides are the first oxidation products of polyhydric alcohols. All of these compounds are very easily oxidized. According to Elmaci et al. (2017) nano-manganese ferrite-supported manganese oxide catalyst can oxidize benzyl alcohol and benzaldehyde without employing any oxidizing agent other than the air present in the reactor. Similar results were obtained by Massa et al. (2012). As demonstrated by Wieland et al. (1996) CO_2, glycolic acid, and adsorbed CO are identified as reaction products for ethylene glycol and glycolaldehyde oxidation by platinum. According to Giroto et al. (2010) the photodegradation of poly-ethylene glycol (PEG) and aqueous solutions by means of photo-Fenton and H_2O_2 / UV processes forms acetic, formic and glycolic acid.

One f the reasons for a better discolouration of a dyestuff solution in acidic media is possibly the increase of MnO_2 reduction potential. Reduction potential of Mn oxides is changed according to the Nernst equation:

$$\beta\text{-}MnO_2(s) + 4\,H^+ \rightarrow Mn^{2+}(aq) + 2\,H_2O \quad E^0(MnO_2/Mn^{2+}) = 1.23\,V$$

In accordance with the Nernst equation, pH reduction increases the reduction potential of Mn oxides. Another reason for a better decolourization in an acidic media is the surface exchange, protonation / deprotonation of Mn oxide with pH. In the common case when the surface charge-determining ions are H^+/OH^-, the net surface charge is affected by the pH of the liquid in which the solid is submerged. The pH (at 25°C) of the isoelectric point for manganese (IV) oxide in water is 4-5. At pH values less than 4-5, the surface of MnO_2 is positively charged and in these conditions the attractive forces between the anionic dye molecules and positively charged MnO_2 particles surface enhance the diffusion of dye molecules from the bulk solution to the adsorbent surface. A third reason may be protonation of negatively charged dye sites, causing hydrophobicity increase of the dye molecules and possibly an easier degradation of such molecules. A possible reason is the fact that pH has an influence on the azo-hydrazo equilibrium of azo dyes. Acidic pH favours the hydrazo form (NH), while basic pH favours the more stable azo form (OH). In magenta dyes this plays an important role (Fryberg, 2005).

To establish a pH-dependent flocculation stability of ink jet dye in this study a pH-adjusted control was prepared. The pH 2 of dyestuff solution did not show any evidence of flocculation but after several months discolourization of magenta occurred, which was more pronounced under the light.

3.2. Oxidation by ultrasonic irradiation

Figure 4 shows the TOC concentration of the dyestuff solution after ultrasonic irradiation. TOC concentrations are similar to those obtained by greensand treatment, and a slight decrease in concentrations was observed regardless to the initial pH value and used power of ultrasound.
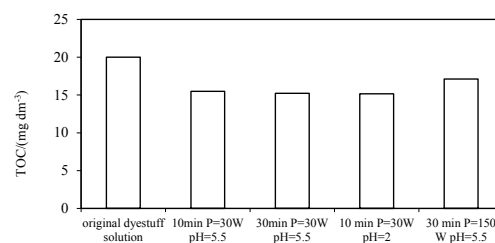

Fig.4.

From the absorption spectra of the dyestuff solution, a very low reduction of the absorption maximum in dyestuff solutions with initial pH

Degradation of inkjet ink by greensand and ultrasonic sonification

5.5 can be seen (Figure 5A) as well as a decrease of absorption maximum after the ultrasonic irradiation in acidic solution (Figure 5B).
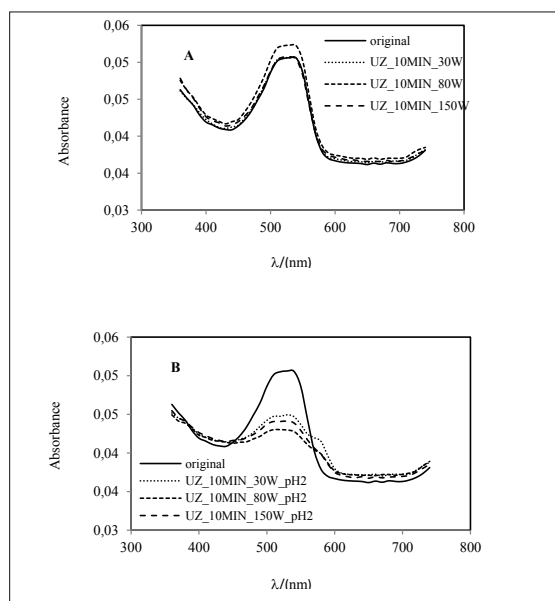

Fig.5.

Therefore, the results are very similar to those obtained after treatment with greensand. In acidic solution, a better decolourization is achieved. Table 4 shows the results of HPLC analysis. It is evident that after the treatment of dyestuff solutions with pH 5.5, the colour

of the solution is not reduced (the number of peaks 6), as confirmed by the spectral absorption curves.

Moreover, peaks surface areas were again slightly higher. After processing of dyestuff solution with pH 2, peaks # 6 disappear. Decolouration efficiency increased in acidic conditions, which was probably associated with the effect of protonation of negative charges in acidic medium and the hydrophobic character of the resulting molecule which enhanced its reactivity (Wu, 2013).

Table 5 shows the share of individual component degradation to the relative analyzed peak areas in the original dyestuff solution. The highest reduction of the peak surface areas was obtained for the peaks # 4-5, and 10-17 in the neutral and acidic dyestuff solutions (from 75 to about 95%). Therefore, the degradation effectiveness of these components is slightly better compared to treatment with greensand. The remaining components # 18 and 19 degrade in a percentage of approximately 55 to 63%, which is similar to that obtained after treatment with greensand. The total area of the peaks present in the original dyestuff solu tion decreased at high ultrasonic irradiation power of 30 W and at pH 5.5 and at pH 2 (10 minutes) as well as

Table 4

Peak No.		Retention time /min	Peak surface areas						
			Original dyestuff solution	pH 5.5 P=30W	pH 2 P=30W	10 min pH 5.5 P=80W	10 min pH 2 P=80W	10 min pH 2 P=150W	30 min pH 5.5 P=150W
1	**A**	**1.3**	**0**	**0**	**197.5**	0	244.5	145.8	0
2	D	2.05	0	93.5	104.1	0	103.4	62.2	0
3	D	3.1	0	41.5	64.1	118.1	13.5	53.4	23.9
4	I	3.8	26.5	0	0	88	0	11.3	13.1
5	I	4.7	649	0	0	47.6	0	10.8	0
6	I (D)	11.9	115.6	119.9	0	124	0	0	120.3
7	D	16.4	0	35.6	0	26.6	36.1	44.7	38,7
8	D	23.5	0	300.2	350.6	306.6	316	322	320.9
9	D	24.5	0	0	51.4	28.3	28.9	29.2	29.9
10	I	25.4	137.1	49.8	49.4	49.9	54.2	52	65.0
11	I	26.5	1162	436.1	374.1	377	356.9	364.6	389.4
12	I	27.1	60.5	0	0	25	26.1	26.6	26.7
13	I	27.7	60.9	0	0	24.3	25	25.2	24.7
14	I	28.5	292	97.5	94.6	102	104	107.6	105.2
15	I	29.1	862.2	193.4	257.4	201.8	206.7	211.3	209.0
16	I	29.5	931.7	0	0	48.8	50.5	51.8	51
17	I	31.5	891.2	130.8	51.6	133	136.2	131.1	126.9
18	I	35.5	5705.5	2286.5	2299.8	2349.6	2350.6	2568.7	2500.2
19	I	38.7	3054.2	1136	1140.7	1152.5	1141.7	1136.5	1142.8

Table 5

Peak No.		Retention time /min	% of degradation					
			10 min pH 5.5 P=30W	10 min pH 2 P=30W	10 min pH 5.5 P=80W	10 min pH 2 P=80W	10 min pH 2 P=150W	30 min pH 5.5 P=150W
4	I	3.8	100.0	100.0	-232.1	100.0	57.4	50.6
5	I	4.7	100.0	100.0	92.7	100.0	98.3	100.0
6	I(dye) (D)	11.9	-3.7	100.0	-7.3	100.0	100.0	-4.1
10	I	25.4	63.7	64.0	63.6	60.5	62.1	52.6
11	I	26.5	62.5	67.8	67.6	69.3	68.6	66.5
12	I	27.1	100.0	100.0	58.7	56.9	56.0	55.9
13	I	27.7	100.0	100.0	60.1	58.9	58.6	59.4
14	I	28.5	66.6	67.6	65.1	64.4	63.2	64.0
15	I	29.1	77.6	70.1	76.6	76.0	75.5	75.8
16	I	29.5	100.0	100.0	94.8	94.6	94.4	94.5
17	I	31.5	85.3	94.2	85.1	84.7	85.3	85.8
18	I	35.5	59.9	59.7	58.8	58.8	55.0	56.2
19	I	38.7	62.8	62.7	62.3	62.6	62.8	62.6

at pH 2 dyestuff solution under irradiation power of 80 W (10 minutes). The surfaces were reduced to 4450, 4267.6 and 4452 (by 68, 69.4 and 68%, respectively). In other cases, the reduction of the peak surface areas is about 66%. The resulting surfaces formed during degradation in acidic solutions were 3.6% (10 min, P = 80 W) to 4% (10 min, P = 30 W), while in pH 5.5 the dyestuff solutions were in a range from 2.7% (30 min, P = 150 W) to 3.4% (10 min, P = 80 W). Somewhat larger resulting peak surface areas in acidic solution can be again attributed to the degradation of dyes and the formation of its degradation products.

4. Conclusions

Greensand has been proved as an oxidant with similar effectiveness compared to ultrasonic irradiation. In all the tested dyestuff solutions, regardless to the initial pH value, the oxidation of the polyhydric alcohols occurs. During the oxidation of polyhydric alcohols monosaccharides, carboxylic acids and other smaller molecules with few double bonds are probably formed. These compounds have lower UV absorbance or they absorbe at wavelengths below 200 nm, which is very difficult to record because usually the mobile phase absorbs in this area, too. In neutral solutions a poor decolourization is present, which can be improved by acidification. Organic molecules which are coloured and absorb in the VIS electromagnetic spectral range have an expanded system of delocalized

π electrons. Aromatic rings do not react easily without a catalyst and UV radiation. Thus, the cleavage of azo molecules probably occurs between two nitrogen atoms resulting in products with a different retention time and absorbance. Hence, the pH value is very important in inkjet water-based printing inks because it can significantly affect the stability of dyes.

5. References

Aldib, M., 2015. Photochromic ink formulation for digital inkjet printing and colour measurement of printed polyester fabrics. Coloration technology, 131, p. 172.

Cie, C., 2015. Ink Jet Textile Printing. Woodhead Publishing Series in Textiles: Number 161. Woodhead Publishing.

Clarkea, C. E., Kielarb, F., Johnsonc, K. L., 2013. The oxidation of acid azo dye AY 36 by a manganese oxide containing mine waste. Journal of Hazardous Materials, 246– 247, p. 310.

Dang, T.-D., Banerjee, A.N., Tran, Q.-T., R., Sudipta, (2016). Fast degradation of dyes in water using manganese-oxide-coated diatomite for environmental remediation. Journal of Physics and Chemistry of Solids, 98, p. 50.

Das, M., Bhattacharyya, K.G., 2014. Oxidation of Rhodamine B in aqueous medium in ambient conditions with raw and acid-activated $MnO_{2, NiO, ZnO \text{ as catalysts}}$. Journal of Molecular Catalysis A: Chemical, 391, p. 121.

Eren, Z., 2012. Ultrasound as a basic and auxiliary process for dye remediation: a review. Journal of Environmental Management, 104, p. 127.

Eren, Z., Ince N.H., 2010. Sonolytic and sonocatalytic degradation of azo dyes by low and high frequency ultrasound. Journal of Hazardous Materials, 177, p. 1019.

Elmaci. G., Ozer, D., Zumreoglu-Karan, B., 2017. Liquid phase aerobic oxidation of benzyl alcohol by using manganese ferrite supported-manganese oxide nanocomposite catalyst. Catalysis Communications, 89, p. 56.

Fang, L., Hong R., Gao, J., Gu, C., 2016. Degradation of bisphenol A by nano-sized manganese dioxide synthesized using montmorillonite as templates. Applied Clay Science, 132–133, p. 155.

Ferreira, G.R., Costa Garcia, H., Couri, M. R. C., Dos Santos, H.F., C. de Oliveira, L. F., 2013. On the Azo/Hydrazo Equilibrium in Sudan I Azo Dye Derivatives. The Journal of Physical Chemistry A, 117, p. 642.

Fryberg, M., 2005. Dyes for ink-jet printing. Rev. Prog. Color., 35, p. 1.

Giroto, J.A., Teixeira, A.C.S.C., Nascimento, C.A.O., Guardani, R., 2010. Degradation of Poly(ethylene glycol) in Aqueous Solution by Photo-Fenton and H_2O_2/UV Processes. Ind. Eng. Chem. Res., 49 (7), p. 3200.

Guzman-Duque, F., Pétrier, C., Pulgarin, C., Peńuela, G., Torres-Palma, R.A., 2011. Effects of sonochemical parameters and inorganic ions during the sonochemical degradation of crystal violet in water. Ultrasonics Sonochemistry 18, p. 440.

Hao, X., Zhao J., Zhao Y., Ma D., Lu, Y., Guo, J., Zeng, Q., 2013. Mild aqueous synthesis of urchin-like MnOx hollow nanostructures and their properties for RhB degradation.Chemical Engineering Journal, 229, p. 134.

Jiang, L., Liu, L., Xiao, S., Chen, J., 2016. Preparation of a novel manganese oxide-modified diatomite and its aniline removal mechanism from solution. Chemical Engineering Journal, 284 (15), p. 609.

Markovski, J. S., Marković, D. D., Đokić V. R., Mitrić, M., Ristić, M., Onjia, A. E., Marinković, A.D., 2014. Arsenate adsorption on waste eggshell modified by goethite, α-MnO_2 and goethite/α-MnO_2. Chemical Engineering Journal, 237, p. 430.

Massah, A., R., Kalbasi, R. J., Azadi, M., 2012. Highly selective oxidation of alcohols using MnO_2/TiO_2-ZrO_2 as a novel heterogeneous catalyst. Comptes Rendus Chimie, 15 (5), p. 428.

Mohamed, M. M., Othman, I., Mohamed, R.M., 2007. Synthesis and characterization of MnO_x/TiO_2 nanoparticles for photocatalytic oxidation of indigo carmine dye. Journal of Photochemistry and Photobiology A: Chemistry, 191, p. 153.

Moumeni O., Hamdaoui O., Pétrier C., 2012. Sonochemical degradation of malachite green in water. Chemical Engineering and Processing: Process Intensification, 62, p. 47.

Onat, T.A., H. Gümüşdere, T., Güvenç A., Dönmez G., Mehmetoğlu Ü., 2010. Decolorization of textile azo dyes by ultrasonication and microbial removal. Desalination, 255, (31), p. 154.

Rehorek, A., Tauber, M., Gubitz G., 2004. Application of power ultrasound for azo dye degradation. Ultrasonics Sonochemistry, 11, p. 177.

Siddique M., Farooq R., Khan, Z. M., Khan, Z., Shaukat, S.F., 2011. Enhanced decomposition of reactive blue 19 dye in ultrasound assisted electrochemical reactor. Ultrasonics Sonochemistry, 18 (1), p. 190.

Qu, J., Shi, L., He, C., Gao, F., Li, B., Zhou, Q., Hu, H, Shao, G., Wang, X., 2014. Qiu, J., 2014. Highly efficient synthesis of graphene/MnO_2 hybrids and their application for ultrafast oxidative decomposition of methylene blue. Carbon, 66, p. 485.

Vončina Brodnjak, D., Majcen-Le-Marechal, A., 2003. Reactive dye decolorization using combined ultrasound/H_2O_2. Dyes and Pigments, 59, p. 173.

Wang, J., Li, J., Jiang, C., Zhou, P., Zhang, P., Yu, J., 2017. The effect of manganese vacancy in birnessite-type $MnO_{2\ on\ room-temperature\ oxidation\ of\ formaldehyde\ in\ air}$. Applied Catalysis B: Environmental, 204 (5), p. 147.

Wang, Y., Zhang, X., He X., Zhang,W., Zhang X., Lu, C., 2014. In situ synthesis of MnO_2 coated cellulose nanofibers hybrid for effective removal of methylene blue. Carbohydrate Polymers, 110 (22), p. 302.

Wieland, B., Lancaster, J. P., Hoaglund, C. S., Holota, P., Tornquist, W. J., 1996. Electrochemical and Infrared Spectroscopic Quantitative Determination of the Platinum-Catalyzed Ethylene Glycol Oxidation Mechanism at CO Adsorption Potentials. Langmuir, 12 (10), p. 2594.

Wu, T.Y., Guo N., Teh, C.Y., Hay, J.X.W., 2013. Advances in Ultrasound Technology for Environmental Remediation. Dordrecht Heidelberg New York London Springer.

Zhang, T., Delai Sun, D., 2013. Removal of arsenic from water using multifunctional micro-/nano-structured MnO_2 spheres and microfiltration. Chemical Engineering Journal, 225, p. 271.

Zhua, M-X., Wanga, Z., Xub, S.-H., Li, T., 2010. Decolorization of methylene blue by β-MnO_2-coated montmorillonite complexes: Emphasizing redox reactivity of Mn-oxide coatings. Journal of Hazardous Materials, 181, p. 57.

This page was left blank intentionally!

Highly Directional Microstrip Ultra Wide Band Antenna for Microwave Imaging System

Vanaja Selvaraj[1], Poonguzhali Srinivasan[2], Jegadish Kumar.K.J[3], Rahul Krishnan[1], Karunakaran Annamalai[1]

[1] Rajalakshmi Institute of Technology, Chennai, India

[2] Anna University, Chennai

[3] SSN College of Engineering, India

Abstract

This paper presents a novel highly directive ultra-wide band antenna for using in microwave imaging systems. Defected Ground Structure (DGS) is incorporated in the top and side of the ground plane to enhance the bandwidth impedance matching. Subsequently, for the further improvement in the bandwidth, gain and directivity staircase slot and square slot is etched at the bottom and top edge of the square patch plane. The low-frequency performance of the proposed antenna can be achieved by adjusting the gap between the ground and patch plane. The proposed microstrip antenna is fabricated on a Flame Retardant (FR4) plate of laminate substrate with dielectric constant of 4.3. The result shows that a directivity of 2.2-8.4dBi is achieved across a bandwidth from 1.43-8.92GHz. Furthermore, gain, directivity, radiation pattern characteristic and reflection coefficient have also been analyzed at the different resonant frequency.

Keywords: Microstrip antenna, microwave imaging systems, ultra-wideband.

1. Introduction

Nowadays, microwave imaging system is largely applied for medical imaging applications like breast cancer detection, lung cancer detection, detect the damaged brain tissue and brain tumor detection etc. [1-5]. Generally, this imaging system is assembled by a planar rectangular or circular cylindrical microwave antenna array for detecting tumor tissue. Usually, for microwave imaging application ultra-wideband signal is used which has high resolution and penetration characteristics.

In microwave imaging system, highly directional and ultra-wideband antennas are commonly used to transmit and receive the pulse. These pulses are transmitted into the breast tissues using a single antenna or array of antenna. The tumor is detected in the breast tissue on the basis of the considerable dielectric contrast between normal and malignant tissue. High scattering of electromagnetic signal produced in the tumor tissue due to the difference in the dielectric properties such as permittivity and conductivity.

Ultra-wideband (UWB) system can operate in very large bandwidth range by using the signals in short pulse duration. This very short pulse duration of the UWB signal makes it enhanced in spatial resolution and short-range competency. Thus when the signal is applied in radar-based microwave imaging application; the increase in bandwidth really allows the UWB radar imaging system to obtain more facts about the targets. The down-range resolution is associated to the wavelength of the pulse [6]. Usually, the UWB pulse is in 1 ns of pulse period, which is equal to 30cm of wavelength in free space, so that the down-range resolution is 15 cm. For traditional narrow band radar imaging system, the pulse duration is 1 μs, is equal to 300 m of wavelength in free space, therefore the down-rage resolution is 150m. Clearly, the reduction of the pulse duration increases the down-range resolution. In the meantime, if the

wavelength of the pulse is larger than the size of the tumor, then the return signal will provide little information about the target [7-8].

There are two approaches for microwave image namely, microwave tomography [9] and radar-based microwave imaging [10-11]. In the radar-based technique, breast is illuminated by a microwave transmitter and the scattered waves are received by the receiver and then reconstructed into an image. In tomography, the received scattered waves are examined to reconstruct the permittivity distribution of the breast tissues. Absolutely in microwave imaging process, the antenna is the key part to radiate and receives signals to or from neighboring scattered objects.

A number of designs of ultra-wide band antenna have been proposed to image the breast tissue using microwave imaging systems [12-17]. T-slots are placed in the corner of the parabolic ground plane with an elliptical slot in the circular patch have been established for microwave breast cancer imaging [12]. A circular disc with L-shape ground plane is proposed for UWB microwave imaging system which has unidirectional radiation pattern [13]. Two semi-elliptical-ended arms with shorting bride configuration are proposed for microwave imaging system [14]. An exponentially tapered Vivaldi antenna with corrugations at the edges of the flaring unit is presented for cancer detection system [15]. Further, rotated E-shaped slot [16] and L-shaped slot [17] in the ground plane with square shaped radiating patch is presented for UWB breast cancer detection.

The above-reported microstrip antennas [12-17], demands for UWB microwave imaging systems have the bandwidth at high frequency (>3GHz) and also the directivity is not in the acceptable level.

Generally, in microwave imaging system, the resolution is improved for the high frequency of operation but penetration energy is reduced. Hence there exists a trade-off between the energy of penetration and resolution of the image. Therefore, to increase the penetration depth and to decrease the attenuation of the transmitted microwave wave signal, the designated antenna should have ultra-wideband. Likewise, to localize the tumor in the particular location high directional antenna is essential. High frequencies are highly essential for detecting the tumor at the skin level; whereas low frequencies are more effective in detecting the

tumor at a deeper level [18, 19]. This motivates a new directional UWB antenna.

To improve the above constrictions, this paper introduces a new directional UWB antenna with staircase and square slot which is etched at the bottom and top edge of the square patch plane, that has a low frequency of operation 1.43GHz, with acceptable directivity, and easier to fabricate.

In section II, the configurations of the proposed antennas are discussed. In section III, simulation result such as reflection coefficient, gain, directivity, radiation pattern and current distribution is discussed. In section IV, measured result of the proposed antenna is discussed.

2. Antenna design

The antenna presented in this paper is to be used in a microwave breast imaging system, which may include a three-dimensional (3D) array of the proposed UWB antennas. In a multi-static configuration, each element of the array takes a turn to transmit a microwave signal while the rest of the elements receive the backscatter signals. This process is repeated until all antennas in the array have been used for transmission. Eventually, 3D or 2D images could be formed by analyzing the backscatter data [20, 21].

Fig. 1(a) shows the front view of the square antenna, with the slot of different dimensions in the top and bottom of the patch plane. Different efforts are made in the antenna configuration to improve the bandwidth. First, stair steps are made at the bottom of the radiating patch. Subsequently, square shaped slots are etched at the top of the patch plane. Secondly, to improve the return loss and widening the fringing fields, two slots of width 2.25mm is etched at the side of the ground plane as shown in fig.1 (b).To increase the bandwidth further a rectangular slot was engraved in the top of the ground plane with a length of 1mm and width of 10mm. The ground plane length is 25.7mm from the feed line.

The antenna is fabricated on an FR4 substrate with a relative permittivity of 4.3 and a thickness of 1.6 mm. The feed line has a width of 3.1 mm, which ensures that the antenna is matched to a 50 Ω impedance source. The complete size of the antenna is 63mm x 72mm x 1.6mm. The lower frequency of operation [22] is calculated using the following equation:

$$f_l = \frac{7.2}{2.25 * L + g}$$

(1)

Where, L is the length of the patch

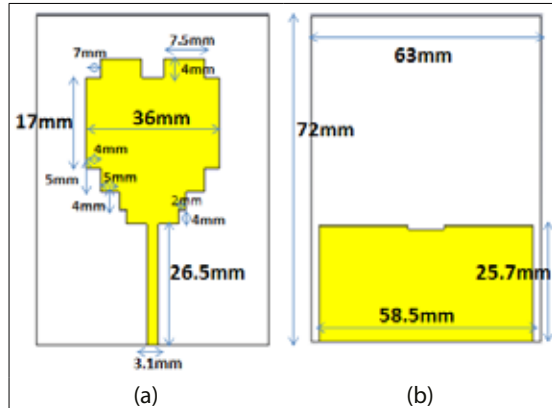g is the gap between patch and ground plane.

Fig. 1 configuration (a) Top view (b) Bottom view

To examine the different antenna properties such as the reflection coefficient, gain, directivity and radiation patterns, the software Computer Simulation Technology (CST) is employed. CST is a professional tool for the 3D electromagnetic simulations of high-frequency devices such as different types of antennas, resonator, filters, couplers, etc. Transient Solver is used to performing the analysis of the different antenna parameters.

3. Results and discussion

In the following section, the simulated properties of the proposed antenna such as reflection coefficient, gain, directivity, surface current and radiation pattern of the proposed antenna are explained in detail.
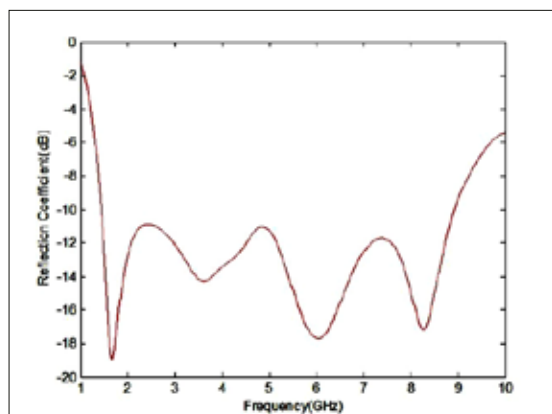
Reflection coefficient

Fig. 2 Simulated reflection coefficient curve of the proposed antenna

The reflection coefficient characteristics of the proposed UWB directional antennas are shown in fig. 2. It is observed from the figure that the proposed antenna covers the bandwidth from 1.43GHz to 8.92GHz which indicates the better impedance matching between the transmission line and antenna.. It is observed that three different resonant frequencies occur at 1.67GHz, 6GHz, and 8.25GHz. It is observed that very low frequency (<1.5GHz) is obtained in the proposed antenna which is very useful for deep penetration in microwave imaging application.

Gain and Directivity

The gain variation plot of the proposed antenna is shown in fig. 3. It is observed that the maximum gain 6.06dB occurs at 6.4GHz. The directivity of the proposed antenna with respect to frequency is shown in fig. 4. It is noticed that directivity increases as the frequency increases and the maximum directivity 8.37dB are obtained at a frequency of 9.8GHz.
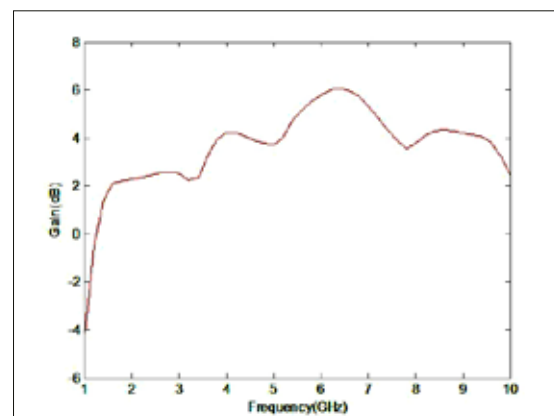

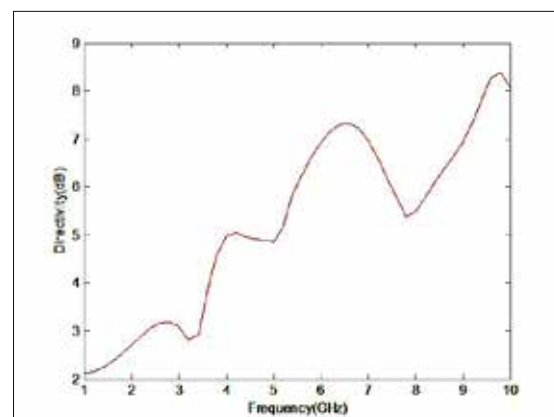**Fig. 3 Simulated gain of the proposed antenna**

Fig. 4 Simulated directivity of the proposed antenna

Radiation pattern

The simulated radiation patterns in x-z plane (H-plane) and x-y plane (E-plane) at different frequencies is shown in Fig. 5. The main aim of the radiation patterns is to illuminate the antenna actually radiates the electromagnetic signal over a wide range of frequency band.

In 3D Radiation Pattern, the entire field distribution with respect to a spherical coordinate system (x,y,z) is analyzed. Whereas in 2D Radiation Pattern, cutting a plane at the center evaluate the rectangular coordinate system. The H-plane radiation pattern is roughly in dumbbell shape, whereas the pattern in the E-plane is butterfly as expected. As frequency is increased the main lobe is becoming more and more directive and it is narrower with an increase in the number of side lobes. The side lobes have increased in number with a corresponding decrease in their magnitude levels. The directions of the lobes also change with frequency, increasing in elevation.
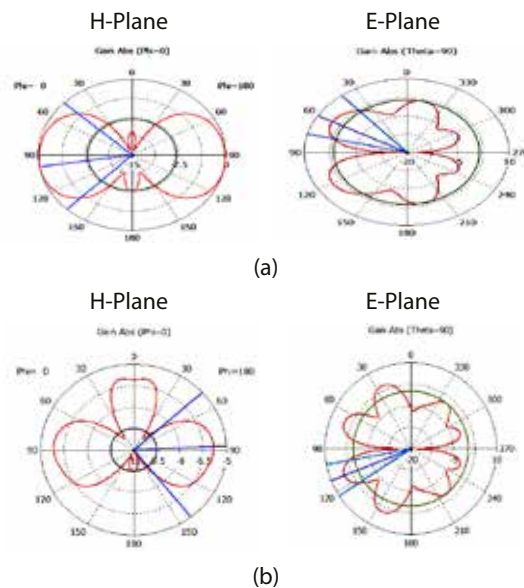

(a)

(b)

Fig. 5 Simulated radiation pattern of antenna. (a) 5.5GHz and (b) 8GHz

The 3-D radiation pattern of the modified square antenna structure is shown in Fig.6.It is noted that the antenna's behavior is same as an omnidirectional antenna in the frequency range below 3.4GHz. The 3-D radiation pattern at 1.4GHz and 2GHz is shown in fig. 6 (a) and fig. 6 (b). The antenna behaves like directional and high gain antenna above 3.4GHz. The 3-D radiation pattern at 5.5GHz and 8GHz is

shown in fig. 6 (c) and fig. 6(d). The antenna has high gain and directivity at 5.5GHz while some distortion and low gain at 8GHz.

In order to penetrate through the body a narrow pulse is transmitted from a UWB antenna. When the pulse propagates through different layers of tissues, reflections and scattering of signal will occur at the interfaces. A specific interest is in the scattered signal from a small sized tissue signifying a tumor. The reflected and scattered signals from the breast tissue can be collected by using a UWB antenna, or array of antennas, and used to map different layers of the body. For an exact imaging system with high resolution, the transmitting/receiving UWB antenna should be highly directional.
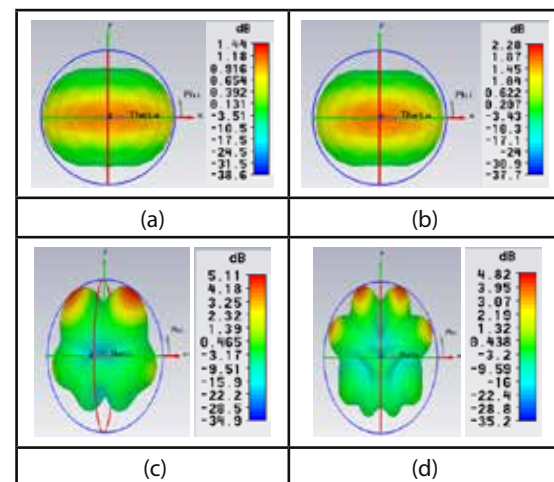

Fig. 6 3-D radiation pattern (a)1.4GHz, (b)2GHz (c) 5.5GHz and (d) 8GHz

Surface current

The distribution of current due to simulation surface of the designed patch antennas with microstrip feed line are shown in fig.7 at different resonating frequency of 2.5GHz, 5.5 GHz and 7.5GHz. The flow of Current is visible along the entire surface of the antenna. Distribution of the current is shown for different frequencies such as 5.5 GHz, 7.5GHz, and 3.5GHz. The simulated results show that the antenna surface current distributed mainly on the edge of the metal patch. The operating frequency of the antenna can be reduced by increasing the path length of antenna surface current. There are two ways to increase the path length: increasing the length and width of the metal patch and cutting the edges of the patch plane. As the frequency

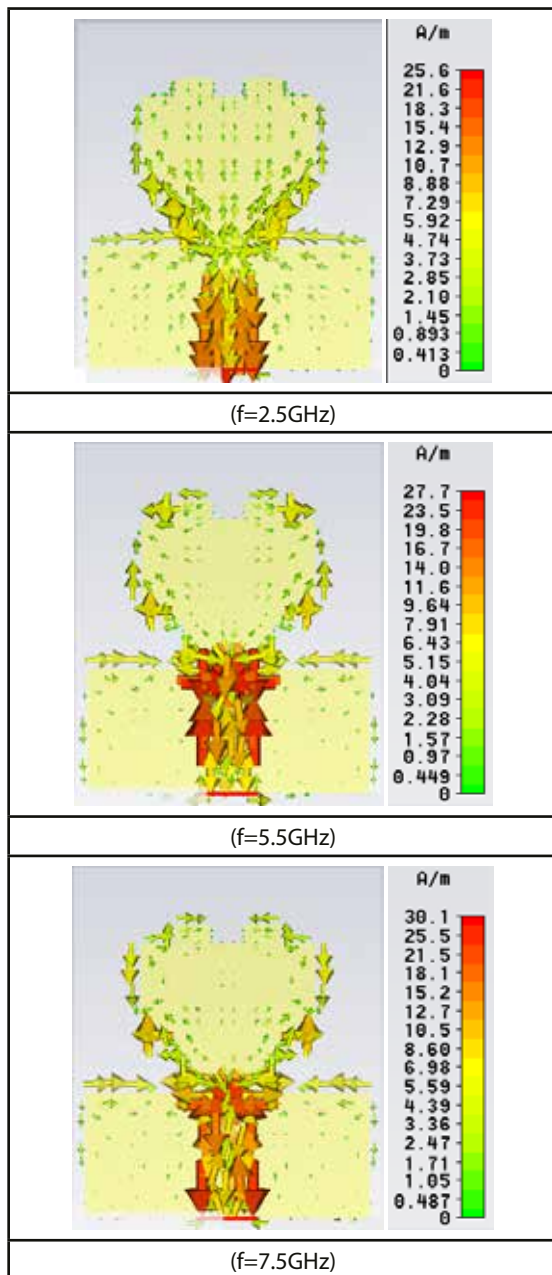of operation increases more amount of current flows through the surface of the antenna.

(f=2.5GHz)

(f=5.5GHz)

(f=7.5GHz)

Fig. 7 surface current of the proposed antenna

4. Fabrication and Measurements

The fabricated antenna is shown in fig. 8. The antenna is fabricated with a height of 1.6mm using a FR4 substrate with 35μm metallization thickness. An SMA connector is soldered at the end of the feed line. The measurement is taken using Vector Network Analyzer having the maximum measurable frequency of 20GHz.

Fig. 8 Photograph of the fabricated antenna

Fig. 9 shows the comparison of measured and simulated reflection coefficient of the designed antenna. The fig.9 shows that there is a good correlation between the simulated and measured result.
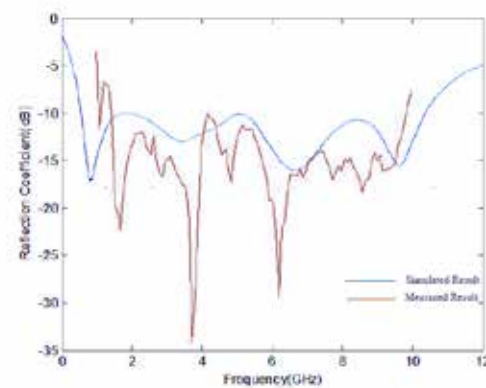

Fig. 9 Measured and simulated reflection coefficient

5. Conclusion

A stripline feed with staircase UWB directional antenna is presented, showing good measured performances over a wide range of bandwidth. The reported antenna faces the impedance bandwidth from 1.43GHz to 8.92GHz. The maximum gain of the proposed antenna is 6.06dB. It is also observed that directivity increases as the frequency increases and the maximum directivity 8.37dB are obtained at a frequency of 9.8GHz. The radiation pattern, surface current, and VSWR have ensured that the proposed antenna would be a promising candidate for a UWB microwave imaging system.

6. Reference

1. Ilhamai Unal, Bahattin Turetken "An Experimental microwave imaging system for breast tumor detection on layered phantom model" (2011)

2. G.Bindu,A.Lonappan "Active microwave imaging for breast cancer detection"(2006)

3.   Zamani, A., S. A. Rezaeieh, and A. M. Abbosh. "Lung cancer detection using frequency-domain microwave imaging." Electronics Letters 51.10 (2015): 740-741.

4.   Chandra, Rohit, and Ilangko Balasingham. "Detection of brain tumor and localization of a deep brain RF-source using microwave imaging." 2015 9th European Conference on Antennas and Propagation (EuCAP). IEEE, 2015.

5.   Mohammed, B. J., A. M. Abbosh, and D. Ireland. "Stroke detection based on variations in reflection coefficients of wideband antennas." Antennas and Propagation Society International Symposium (AP-SURSI), 2012 IEEE. IEEE, 2012.

6.   Bury, Marek, Yevhen Yashchyshyn, and Jozef Modelski. "Improvement of the Microwave Imaging System by Deconvolution of the Antenna Pulse Response." International Journal of Electronics and Telecommunications 56.3 (2010): 209-214.

7.   Borkar, V. G., A. Ghosh, R. K. Singh, and N. K. Chourasia. "Radar cross-section measurement techniques." Defence Science Journal 60.2 (2010): 204.

8.   Niu, Ruixin, Rick S. Blum, Pramod K. Varshney, and Andrew L. Drozd. "Target localization and tracking in noncoherent multiple-input multiple-output radar systems." IEEE Transactions on Aerospace and Electronic Systems 48.2 (2012): 1466-1489.

9.   Grzegorczyk, Tomasz M., Paul M. Meaney, Peter A. Kaufman, and Keith D. Paulsen. "Fast 3-D tomographic microwave imaging for breast cancer detection." IEEE Transactions on Medical Imaging 31.8 (2012): 1584-1592.

10. Burfeindt, Matthew J., Nader Behdad, Barry D. Van Veen, and Susan C. Hagness. "Quantitative microwave imaging of realistic numerical breast phantoms using an enclosed array of multiband, miniaturized patch antennas." IEEE antennas and wireless propagation letters 11 (2012): 1626-1629.

11. Burfeindt, Matthew J., Timothy J. Colgan, R. Owen Mays, Jacob D. Shea, Nader Behdad, Barry D. Van Veen, and Susan C. Hagness. "MRI-derived 3-D-printed breast phantom for microwave breast imaging validation." IEEE antennas and wireless propagation letters 11 (2012): 1610-1613.

12. Meena, M. L., Mithilesh Kumar, and Girish Parmar. "Modified Unidirectional Circular Patch Antenna with Parabolic Shape Ground Plane Having T-Slots for Microwave Links." ICTACT International Journal on Communication Technology 6.2 (2015): 1087-1090.

13. Islam, M. M., Mohammad Tariqul Islam, M. Samsuzzaman, Mohammad Rashed Iqbal Faruque, and Norbahiah Misran. "Omni-directional microstrip monopole antenna for UWB microwave imaging system." Computer, Communications, and Control Technology (I4CT), 2015 International Conference on. IEEE, 2015.

14. Low, Xue Ni, Zhi Ning Chen, and Terence SP See. "A UWB dipole antenna with enhanced impedance and gain performance." IEEE Transactions on Antennas and Propagation 57.10 (2009): 2959-2966.

15. Pandey, G. K., H. S. Singh, P. K. Bharti, A. Pandey, and M. K. Meshram. "High Gain Vivaldi Antenna for Radar and Microwave Imaging Applications." International Journal of Signal Processing Systems 3.1 (2015): 35-39.

16. Ojaroudi, N., and N. Ghadimi. "Omnidirectional microstrip monopole antenna design for use in microwave imaging systems." Microwave and Optical Technology Letters 57.2 (2015): 395-401.

17. Song, Kun, Ying-Zeng Yin, Shou-Tao Fan, and Bo Chen. "Compact open-ended L-shaped slot antenna with asymmetrical rectangular patch for UWB applications." Progress In Electromagnetics Research C 19 (2011): 235-243.

18. Chang, Dau-Chyrh, Yau-Jyun Tsai, Chih-Hung Lee, and Chang-Hsuan Kao. "Tradeoff study of microwave imaging based on frequency considerations." Session 4P4b Novel Optical Imaging Methods for Biomedical Applications, Spectroscopic and THz Bioelectromagnetics (2014): 1946.

19. Peng, Jing, Juming Tang, Yang Jiao, Stewart G. Bohnet, and Diane M. Barrett. "Dielectric properties of tomatoes assisting in the development of microwave pasteurization and sterilization processes." LWT-Food Science and Technology 54.2 (2013): 367-376.

20. Hagness, Susan C., Allen Taflove, and Jack E. Bridges. "Three-dimensional FDTD analysis of a pulsed microwave confocal system for breast cancer detection: Design of an antenna-array element." IEEE Transactions on Antennas and Propagation 47.5 (1999): 783-791.

21. Zainud-Deen, Saber Helmy, Walaa M. Hassen, E. M. Ali, Kamal Hassan Awadalla, and H. A. Sharshar. "Breast cancer detection using a hybrid finite difference frequency domain and particle swarm optimization techniques." Radio science conference, 2008. nrsc 2008. national. IEEE, 2008.

22. Ray, K. P. "Design aspects of printed monopole antennas for ultra-wide band applications." International Journal of Antennas and Propagation 2008 (2008).